ALMA MATER STUDIORUM · UNIVERSITÀ DI BOLOGNA

Looking for silicene: studies of silicon deposition on metallic and semiconductor substrates

Relatore: Presentata da:

Dott. Luca Pasquini   Alberto Curcella

Supervisore dell' internship:

Dott. Geoffroy Prévot
(UPMC - Paris VI)

It's barely yours on loan,
what you think you own.
The place that you call home,
the ideas in your bones.
In your bones.

Contents

Abstract

Nel presente lavoro espongo i risultati degli esperimenti svolti durante la mia internship all'Institut des NanoSciences de Paris (INSP), presso l'Università Pierre et Marie Curie (Paris VI), nel team "Phisico-Chimie et Dynamique des Surfaces", sotto la supervisione del Dott. Geoffroy Prévot. L'elaborato è stato redatto e integrato sotto la guida del Dott. Pasquini, del dipartimento di Fisica e Astronomia dell'Università di Bologna. La tesi s'inserisce nel campo di ricerca del silicene, i.e. l'allotropo bidimensionale del silicio. Il cosidetto free-standing silicene è stato predetto teoricamente nel 2009 utilizzando calcoli di Density Functional Theory, e da allora ha stimolato un'intensa ricerca per la sua realizzazione sperimentale. La sua struttura elettronica lo rende particolarmente adatto per eventuali applicazioni tecnologiche e sperimentali, mentre lo studio delle sue proprietà è di grande interesse per la scienza di base.

Nel **capitolo 1** presento innanzitutto la struttura del silicene e le proprietà previste dagli studi pubblicati nella letteratura scientifica. In seguito espongo alcuni dei risultati sperimentali ottenuti negli ultimi anni, in quanto utili per un paragone con i risultati ottenuti durante l'internship.

Nel **capitolo 2** presento le tecniche sperimentali che ho utilizzato per effettuare le misure. Molto tempo è stato investito per ottenere una certa dimistichezza con gli apparati in modo da svolgere gli esperimenti in maniera autonoma.

Il **capitolo 3** è dedicato alla discussione e analisi dei risultati delle misure, che sono presentati in relazione ad alcune considerazioni esposte nel primo capitolo.

Infine le **conclusioni** riassumono brevemente quanto ottenuto dall'analisi dati. A partire da queste considerazioni propongo alcuni esperimenti che potrebbero ulteriormente contribuire alla ricerca del silicene. I risultati ottenuti su Ag(111) sono contenuti in un articolo accettato da Physical Review B [1].

Chapter 1

About silicene

This chapter is mainly aimed to give a general overview about silicene. In the last years a great effort has been invested in research in order to better characterize it from a theoretical point of view and, of course, try to observe it experimentally. The main features expected shall be presented along with the state-of-art of research in this field, focusing mainly on the experimental aspects. In many cases, the theoretical investigation requires usually a thorough knowledge of Density Functional Theory (DFT). Its description doesn't belong to the aim of the present work. Anyway, the results of DFT calculations will be used in order to provide a description of the properties predicted for silicene.

1.1 Introduction

Since the first observation of graphene in 2004 [2], a lot of interest has been focused on its characterization and on its possible applications in technological devices. Indeed, this global commitment is well-founded as this 2-D sheet of honeycomb arranged carbon atoms shows exotic properties, such as linear electronic dispersion, scalability to nm sizes, ballistic transport, linear I-V characteristic, sustainable currents higher than 10^{-8} A/cm^2 and eventually it is a zero gap semiconductor, which explains its metallic-like behaviour. Nevertheless, along with this discovery several research groups around the world have begun to wonder whether a 2-D arrangement of atoms was possible also for other atomic species of

Figure 1.1: Predicted silicene structure: due to the buckling the Si atoms in the A sites and in the B sites lay onto two different planes separated by Δ_{LB}=0,44 Å. d_{Si-Si} is predicted to 2.25 Å by Cahangirov et al. [5]. The unit cell and the basis vectors are shown in the figure, too.
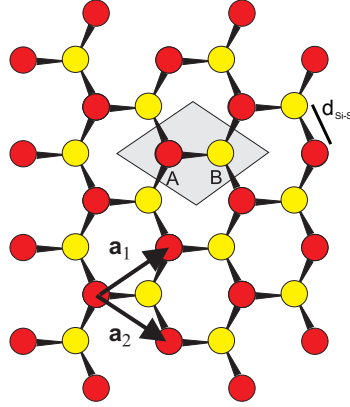
the 14th group, especially for silicon and germanium. In analogy with graphene they shall be addressed to as silicene and germanene, respectively. Thus, in the last years theoretical investigations have predicted stable bi-dimensional configuration for this kind of materials assumed they could actually be obtained in laboratory [3–5,7]. Comparing silicon and germanium with carbon, an important difference emerging is the tendency to form sp_2 hybridization for the latter, and sp_3 in the case of the first two materials. Our attention will focus on silicene, for which calculations have shown it should present similar properties to the ones observed for graphene, as the linear dispersion and zero gap at the Brillouin zone corners, resulting in high-efficiency electronic transport. Thus, all the possible technological implementations studied for graphene would suit also for silicene with the non negligible advantage of being already compatible with existing semiconductor technologies [3]. An heavy drawback of silicene and germanene, which is also the reason why observing them is such a difficult task, is that layered structure of these materials, as graphite is for graphene, have never been observed in nature.

Moreover, the impact on the market following eventually this discovery has not to be underestimated. Just consider that in 2014, the global market of graphene has reached USD 15-20 millions [8], with most sales in semiconductor electronics, energy batteries and composite material industries. For the reasons listed above silicene appears to be of great interest both for fundamental research and industry applications.

4

1.2 Properties of silicene

In this section an overview of the most remarkable properties of silicene shall be given, trying to put in evidence drawbacks and advantages in comparison with graphene. DFT calculations done by Cahangirov et al. [5] investigate the equilibrium structure of silicene and discuss, in particular, planar (PL), low-buckered (LB) and high-buckled (HB) honeycomb arrangements. The PL structure results to be the least energetic configuration, but it is not stable as it presents phonon modes with imaginary frequencies.
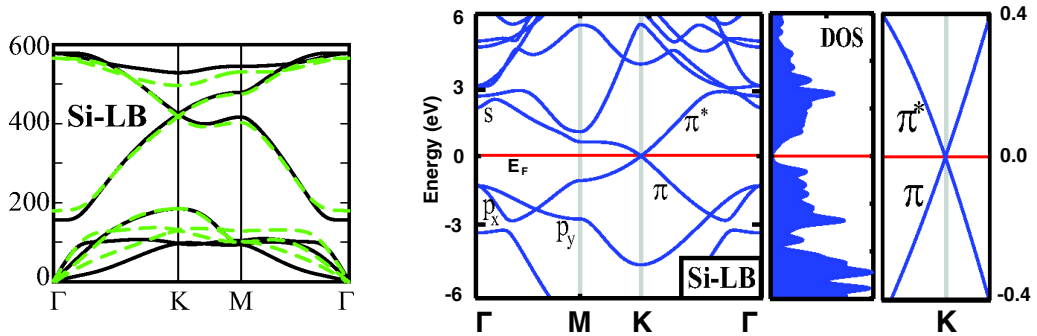
(a) Phonon dispersion for PL and LB silicene. Black and green curves are obtained using two different DFT models. The general trend is retained.

(b) Electronic dispersion, DOS and focus onto the K-point for LB silicene. s, p_x, p_y orbitals trends are indicated.

Figure 1.2

These imaginary frequencies can be interpreted as a dissipation of the energy which causes the instability of the system. The phonon dispersion is shown in figure 1.2(a) [5] in the case of a buckling $\Delta_{LB} = 0{,}44$ Å, for which optical branches have positive frequencies. At the center of the first Brillouin zone (FBZ) one can observe a linear trend of the acoustical branches. Moreover, the calculations show that the structure is stable in a temperature range quite wide, that is 0 K $\leq$ T $\leq$ 1000 K. The most stable structure is found to have a buckling $\Delta_{LB} = 0{,}44$ Å and a Si-Si distance of $2{,}25$ Å. In figure 1.2(b) [5] the electronic dispersion calculated for LB silicene is presented next to the corresponding density of states (DOS). The most striking feature is the crossing of the π- and π^*-bands at the K and K′ symmetry points of the FBZ, where, moreover, E=E$_F$. This means that silicene

is predicted to have a semi-metallic behaviour, i.e. it is a zero-gap semiconductor. On the very right side of figure 1.2(b) it is shown also a focus on the K-point at the Fermi energy. The evident linear trend implies that electrons near this symmetry point act like massless Dirac Fermions. Fitting the linear trend in the proximity of the K- and K′-point, one estimates the Fermi velocity:

$$v_f \simeq \boldsymbol{E}(\boldsymbol{q})/\hbar|\boldsymbol{q}| \tag{1.1}$$

DFT calculations predict a velocity of $\sim 10^6$ m/s [5], while a tight-binding approach leads to $\sim 10^5$ m/s, that is lower than the one found in graphene (2,5 10^6 m/s [6]). It has been argued that this is due to the π-bonds, responsible for the conduction inside the sheets, which are weaker in silicene than graphene [4]. Another remarkable consideration pointed out by Cahangirov et al. is that LB

Figure 1.3: Left: ideal and relaxed structure of Si NRs. In the latter, the (2x1) asymmetric reconstruction can be observed at the edges. Right: variation of E_G as a function of the width n of the NRs, showing an oscillatory trend.
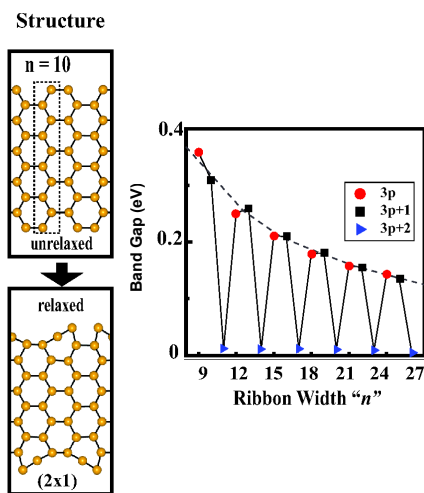
silicene is ambipolar in the region close to the Fermi level.

Concerning eventual applications, nanoribbons (NRs) of silicene would be of great interest [3]. It is predicted that for n>7, being n the width of the ribbons in terms of number of Si atoms, the structure still shows a LB honeycomb pattern. Considering an armchair arrangement, figure 1.3, the objects appear to be a non-magnetic semiconductor with a non-zero band gap [5]. Of course the quantum confinement effect results in an increase of E_G with decreasing values n. Anyway, it can be observed from the plot in figure 1.3 that, just as in graphene, the band

6

gap shows an oscillatory behaviour as a function of n. The remarkable property of gap engineering can lead to the creation of quantum dots and multiple quantum wells.

Another interesting comparison between graphene and its silicon counterpart is the defects formation. A very common feature one has to deal with when growing ultra-thin films of atoms arranged in honeycomb pattern is the Stone-Wales (SW) defect.
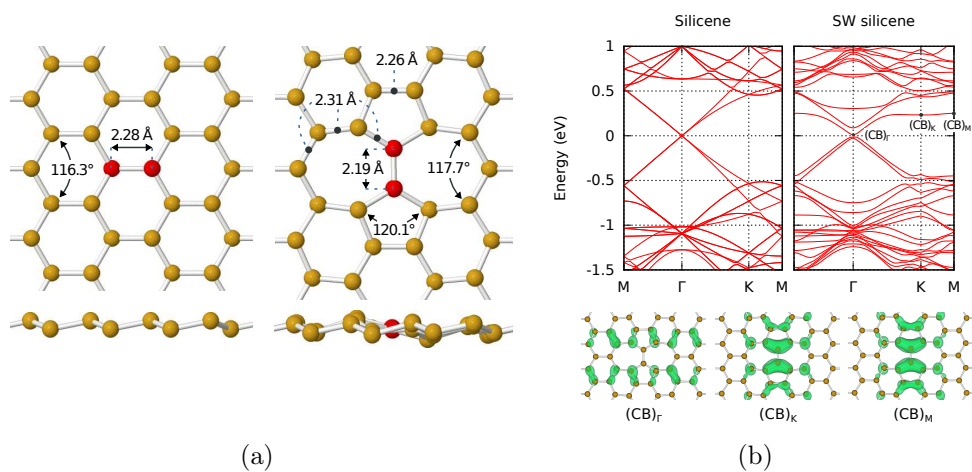

Figure 1.4: (a) structure of free standing silicene and relative calculated equilibrium distances, in the absence (left) and presence (right) of SW defects. (b) Dispersion curves associated to the structures in (a), top left and top right respectively. On the bottom are plotted the charge densities of the conduction band near the Fermi energy at high symmetry points of the FBZ. [9]

This defect consists in the 90° rotation of two bounded atoms of the layer, which results in the formation of two heptagons and two pentagons surrounding the rotated couple, figure 1.4(a). The potential barrier for the formation of defects is substantially smaller in silicene compared to graphene, $\sim$2,4 eV and $\sim$9,2 eV respectively. Moreover, the inverse process, that is the relaxation of the defects, still shows a potential barrier of $\sim$0,76 eV, which guarantees the stability of such defects also at modest temperatures [9]. The dispersion curves for ideal and SW silicene are plotted in figure 1.4(b). The K and K$'$ symmetry points are folded onto the Γ point. The most interesting effect of the presence of defects in the layer is that a gap is opened in the vicinity of the Dirac point. Its value depends on the concentration of defects; for example, considering a 6x6 supercell with a defect concentration of 1,9 10^{13} cm^{-2} the gap is calculated to be 0,02 eV. These considerations can be pushed more forward speculating about the possibility of doping in the presence of defects. In particular Sahin et al. [9] prove that the doping of silicene with N atoms transform the classical semi-metallic material into a ferromagnetic metal with total magnetization 1,0 μ_B.

More properties, even more exotic than the ones cited, have been predicted and are still investigated, but their description lies outside the general purpose of this work.

1.3 Experimental observations of silicene

The first claim of an experimental observation of silicene dates back to 2010. The first studies dealt mainly with silicon deposition on Ag(110) and Ag(111), for which a description will be given. Nevertheless, it is worth noting that the electronic properties showed by silicon deposited on metal surfaces are altered by strong silicon-metal interaction, which makes questionable the silicene nature of the structures studied. In particular in this section and in the next chapter, the possibility of a misleading interpretation of some results obtained in the last years will be discussed, concerning the presumed observation of epitaxially grown silicene sheets on Ag(111) and MoS$_2$ [10, 25] and silicene NRs on Ag(110) [11].

1.4 Silicene nanoribbons (NRs) on clean Ag(110)

It has been observed that the deposition of silicon onto a clean Ag(100) results in the formation of one dimensional silicene structures, i.e. nanoribbons, well aligned along the (-110) direction and with a characteristic width of 16 Å [11, 12]. It has been reported that changing the substrate temperature, NRs form with different widths, i.e. 0,8 and 1,6 nm figure 1.5 [14].
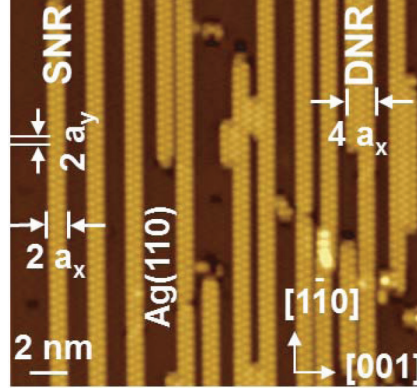

Figure 1.5: Single nanoribbons (SNR) of ∼0,8 nm, and double nanoribbons (DNR) of 1,6 nm of width. a_x and a_y are the basis vector of the Ag surface.

It has been reported [12] that performing evaporation with a substrate temperature of 230 °C a better structural ordering can be obtained. In figure 1.6(a) filled-states STM image is presented next to the model for its description. The shortest distance between protrusions is 0,335 nm, much larger than the expected 0,235 nm for bulk silicon [3] or 0,225 nm for silicene [5], from which it can be argued that it doesn't represent the Si-Si distance. Assigning this protrusions to the second neighbour atoms, the more realistic silicon distance of 0,193 nm is obtained, figure 1.6(b). Thus, assuming that not all the atoms are resolved in the STM images, a realistic model is obtained. Nevertheless, two recent works [14, 15] undermine the hypothesis of the silicene nature of the NRs mentioned above, when they cover completely the silver substrate. Bernard et al. have observed, by means of grazing incident X-ray diffraction (GIXD) and STM studies, that the silicon deposition induces a reconstruction of the Ag substrate, despite the non-miscibility of the two-elements. Moreover, Borensztein et al. exploit surface differential reflectance spectroscopy to observe important differences between the absorption predicted for
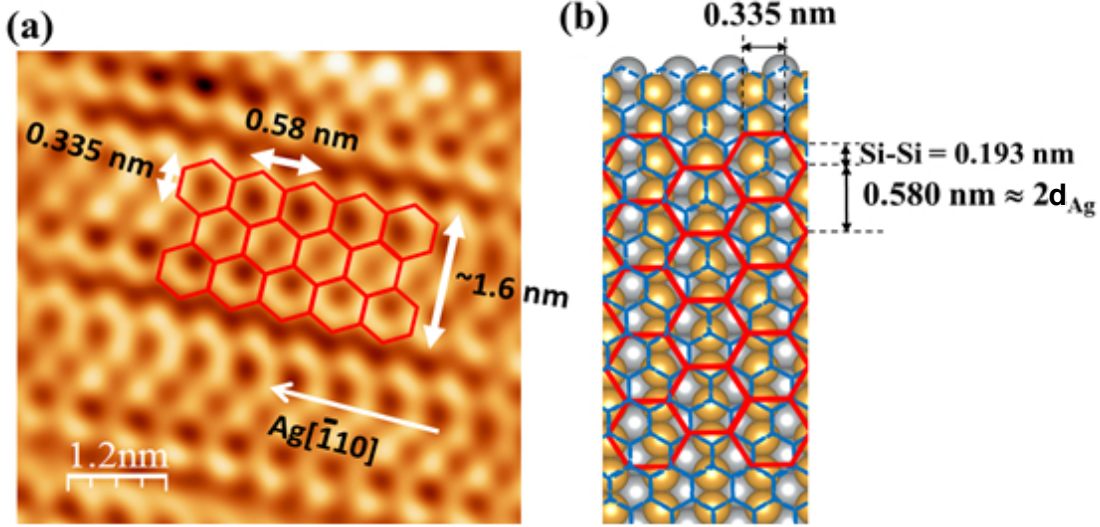
Figure 1.6: (a) Filled-state image of silicene NRs grown at 230 °C on Ag(110) (6x6 nm^2, V=-0,2 V, I=1.9 nA). (b) Proposed model to interpret the STM images of Si NRs: the red honeycomb net represents the Si atoms evident in the acquired images; the blue net represents the actual configuration of the silicon atoms. It seems reasonable to think that the non-resolved atoms are the buckled ones in the NRs structure.

silicene and the one observed for the NRs. Thus, these two last observations make highly questionable the silicene nature of the nanoribbons, as silver contribution in the assembling process cannot be excluded.

1.5 Silicene growth on Ag(111)

Given the hexagonal close packed arrangement of its atoms and its smooth surface potential [3], the (111) face of the transition metals appears to be ideal for the growth of 2D thin films and sheets. It appears particularly suited for Si deposition, as the two materials are almost non-miscible [16]. Silicon grown on Ag(111) bare substrates has been studied exploiting atomic resolved scanning tunnelling microscopy and LEED [17]. The images obtained show that a rotated honeycomb arrangement of atoms appears on the sample after silicon evaporation, figure 1.8(b). A LEED analysis, figure not shown by Lalmi et al. [17], confirms that this pattern is associated to a $(2\sqrt{3}$ x $2\sqrt{3})$R30° superstructure, leading to

the model shown in figure 1.8(c). It is worth noting that the Si-Si distance found in this study is 0,19 nm, that is 17% shorter than the one in bulk silicon (0,235 nm) [17].
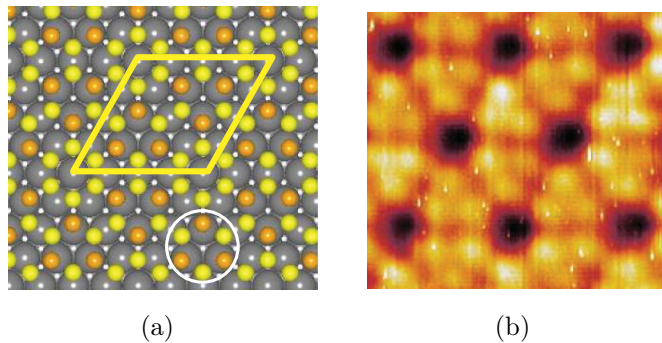

Figure 1.7: (a) Ideal organisation of silicon atoms on Ag(111) in a 4x4 superstructure and corresponding STM image reported (b).

These results, of course, are far from being conclusive regarding the silicene nature of the 2D arrangement observed. In order to prove or disprove this hypothesis, Vogt et al. [19] presented a combined STM and angular-resolved photoemission spectroscopy (ARPES) work, claiming to have observed a linear dispersion at the K-point of the FBZ, after having evaporated silicon on an Ag(111) substrate, from which a Fermi velocity of $1,3 \cdot 10^{-6}$ m/s was deduce, which is even higher than the one reported for graphene. The superstructure observed this time with STM, and confirmed by LEED, showed a 4x4 supercell, figure 1.9(a). Nevertheless, the expected sp band of the bare Ag(111) is not shown and further studies assigned the linear dispersion to the folding of such a band into the FBZ and confirmed that the Dirac cone in the 4x4 silicene phase is destroyed as a consequence of strong Si-Ag interaction [3].

Following the first observation of an epitaxial layer grown on Ag(111), more experiments have been performed, focusing the attention on the role of the temperature of the substrate. It has been observed [20] that employing temperatures above 330 °C no superstructure was observed. On the contrary, at temperatures below this one, an evolution from the (4x4) surface pattern, at T=150 °C, to the $(2\sqrt{3} \times 2\sqrt{3})R30°$, at T=300 °C, was noted. In the range between these temperatures, both phases are present, plus a $(\sqrt{13} \times \sqrt{13})R13,9°$. These considerations
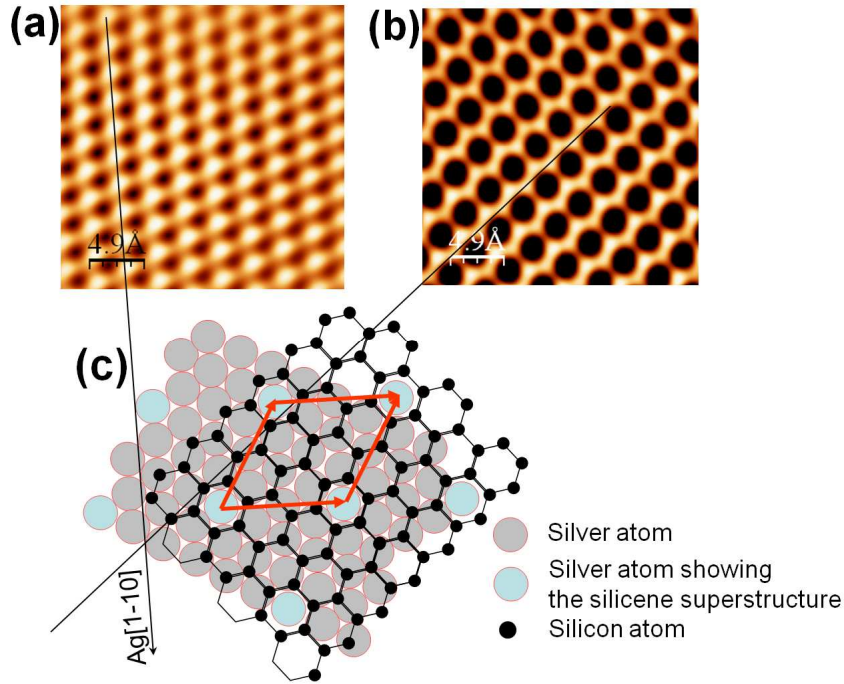
11

Figure 1.8: Filled-state images of the bare Ag(111) substrate (a) and of $(2\sqrt{3}$ x $2\sqrt{3})$R30° superstructure observed after the evaporation of silicon. In (c) it is made more clear $2\sqrt{3}$ ratio between the new lattice vectors (red arrows) and the ones of the hcp silver structure. The rotation between the two honeycomb arrangement is highlighted, too.

are deduced by means of LEED, figure 1.9, and STM measurements performed after the deposition of about 1 ML of silicon.

Concerning the role of the coverage into the reconstructions, it has been observed [21] that maintaining the substrate in the temperature range 200-220 °C, the first layer deposited shows a 4x4 superstructure. Increasing the coverage, a $(\sqrt{3}$ x $\sqrt{3})$ pattern appears to be more and more important until it finally becomes dominant after ~5 MLs deposition. Note that this reconstruction has been never observed for silicon. Just relying on the step height observed for the $(\sqrt{3}$ x $\sqrt{3})$, the superstructure has been interpreted as a silicene monolayer.

Anyway, a recent STM study showed also that the growth of silicene-like sheets on Ag(111) comes along with the release of about 65% of the silver atoms from the Si covered areas [24], showing that the two materials do interact, despite
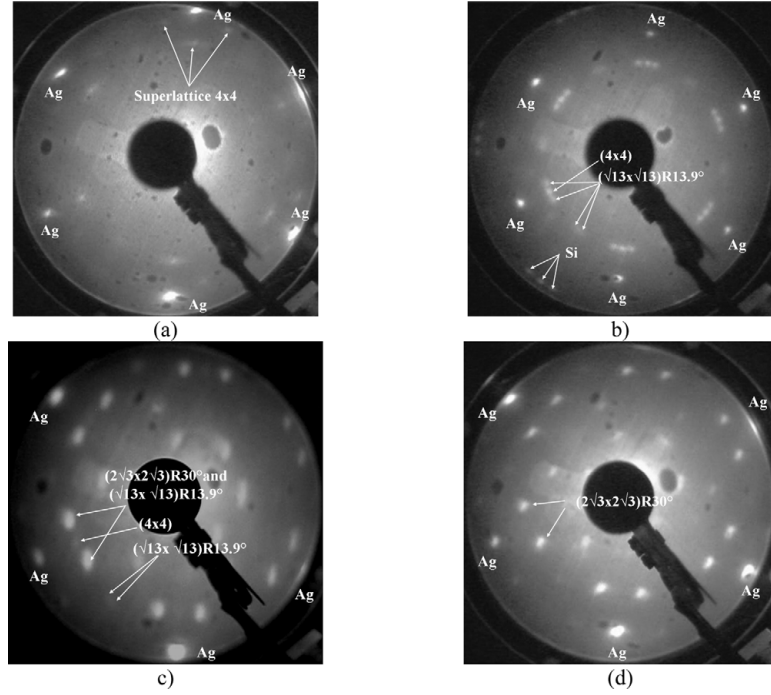
Figure 1.9: LEED images acquired after the deposition of ∼1 ML of silicon on a Ag(111) substrate at different temperatures. (a) 4x4 superstructure, T=150 °C. (b)-(c) spots originating from (4x4), $(2\sqrt{3} \times 2\sqrt{3})R30°$ and $(\sqrt{13} \times \sqrt{13})R13,9°$, respectively at 210 °C and 270 °C. (d) $(2\sqrt{3} \times 2\sqrt{3})R30°$ superstructure.

their immiscibility. In particular large scale STM images show that at the very beginning of Si evaporation at T=167 °C, step edges undergo stabilization and faceting along the ⟨110⟩ direction figure 1.10(a). This is caused by the diffusion of silicon atoms which interact with Ag at the step edges, modifying their shape. Further evaporation causes the nucleation of islands on the terraces and strips at the step edges. At higher coverages, dentritic features develop, which appear very smooth with no atomically resolved structure, figure 1.10(e). The height of these features is 0,236 nm that is exactly the height of a single Ag(111) step, figure 1.10(f). Thus, these features clearly involve silver.

Concerning multi-layers silicene structures, it has been recently argued [22] that long silicon evaporation on a Ag(111) substrate results in the formation of a thin film of bulk-like silicon terminated with the Si(111) $\sqrt{3} \times \sqrt{3}$-Ag surface. LEED analysis shows that after the first monolayer deposition a 4x4 superstructure is

Figure 1.10: Si evaporation on Ag(111) at T=167. (a) clean silver surface. (b) Very beginning of the evaporation: note the faceting of the step edges along the ⟨110⟩ direction. Coverage: 0,09 MLs. (c)-(e) Increasing Si deposition: 0,28; 0,49; 0,74 respectively. (f) Profiles relative to the black line in (a) and the red one in (e).
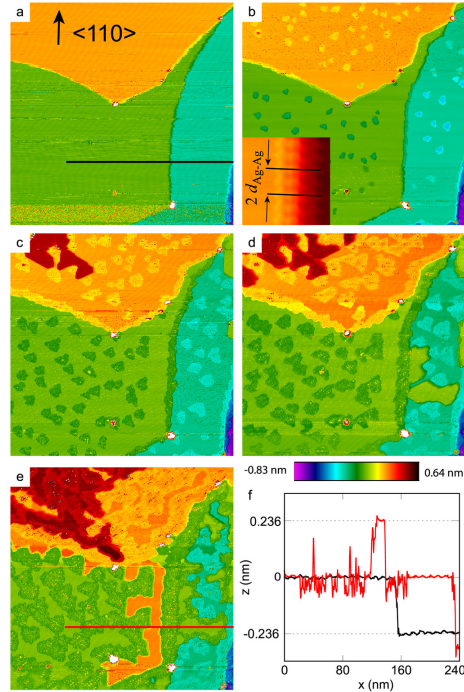
present at the surface. Afterwards, for longer Si evaporation, the ($\sqrt{3}$ x $\sqrt{3}$) spots emerge in the images, in agreement with the previous work. At this point, LEED I-V curves were acquired and compared to the ones calculated for silicene layers, highlighting important differences between them. Thus, it was noted that these IV curves resemble the same kind of curves obtained for Si(111) $\sqrt{3}$ x $\sqrt{3}$-Ag surface. Calculated and experimental result gave this time a good agreement.

As the Ag(111) substrate was made from the deposition of silver onto Si(111), in order to be sure that during the process of annealing no break in the Ag(111) occurred causing the Si(111) $\sqrt{3}$ x $\sqrt{3}$-Ag surface to form, further verifications have been made, excluding this eventuality. Thus, it was concluded that Ag acts as a surfactant in the Si growth process, meaning that silver atoms remain segregated at the surface.

These considerations will be useful in the third chapter when LEED, AES and SDRS results after long silicon evaporation on Ag(111) will be presented.
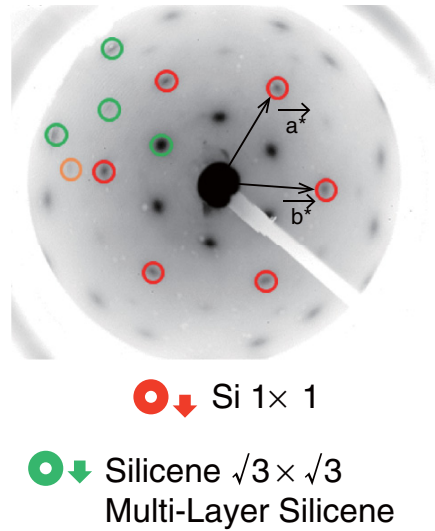
14

Figure 1.11: LEED image acquired after the deposition of ~ 4 MLs of silicon on a Ag(111) substrate. The spots relative to bulk-like silicon are highlighted in red, while in green it has been highlighted the spots of the $\sqrt{3}$ x $\sqrt{3}$ superstructure. The orange circle is associated to the bare silver substrate.

1.6 2D Silicon nanosheets on MoS$_2$

So far it has been showed that the interaction between silver and silicon hampers the silicene nature of the 1D and 2D structures observed after Si evaporation on Ag(110) and Ag(111). Obviously, it is desirable to find a substrate which could provide a template for the growth of silicene, avoiding as much as possible their mutual interaction, so that the Si-induced features could realistically show a silicene nature, not only in the structure, but also in the properties.
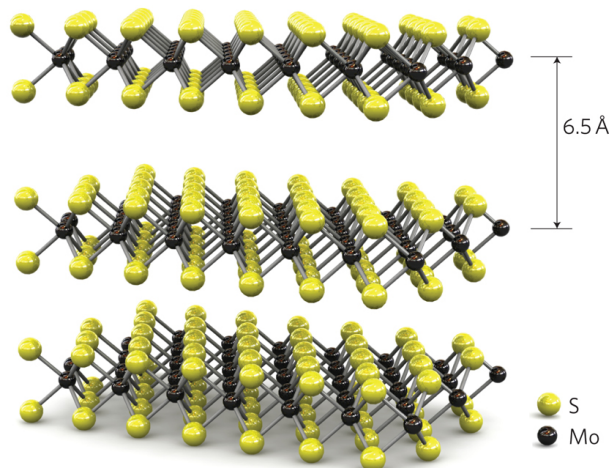

Figure 1.12: MoS$_2$ sandwich stack structure.

Layered graphite-like materials with hexagonal crystal symmetry appear to be promising candidates for such a task, being non-metallic substrates quite suitable for the 2D growth of silicon with an honeycomb arrangement. The cleavage of such layered compounds does not create dangling bonds, making them ideal inert surfaces for van der Waals epitaxy of weakly interacting silicon films [25]. For example, MoS_2 comprises a stack of S-Mo-S sandwiches and the basal surface consists of a chemically-inert layer of sulphur atoms [40]. The absence of orbitals suitable for bondings between the MoS_2 sandwiches accounts for the lack of reactivity of the material. Each molybdenum atom is bonded to three sulphur atoms above and below, figure 1.12.
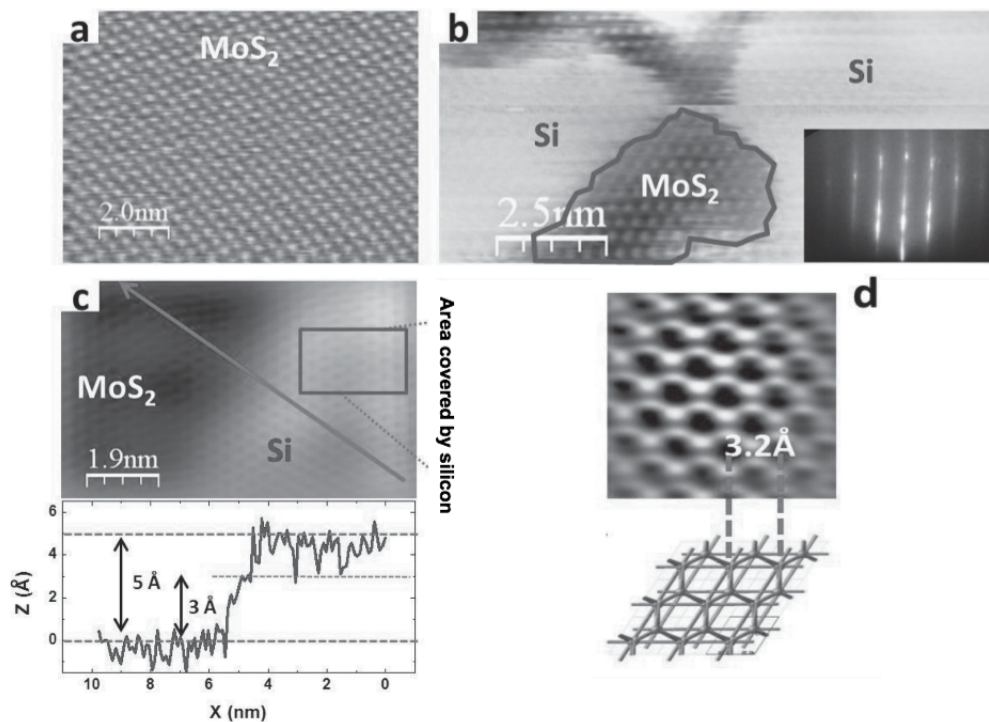
Figure 1.13: (a) Clean MoS_2. (b) Partially covered MoS_2 after 0,8 ML Si deposition and relative RHEED pattern (inset). (c) Image acquired with different parameters (higher bias, lower set current) of a partially covered surface. In the inset is presented the profile taken along the arrow in the STM image. (d) Atomically resolved image acquired onto a silicon covered area and proposed model, in which the honeycomb silicon lattice is superimposed to the one of the substrate.

It is worth showing some results and considerations reported for silicon deposition

on MoS$_2$ held at T=200 °C [25], as this kind of substrate has been employed during this internship and a comparison shall be given in chapter 3. Once obtained a silicon coverage of 0,8 MLs, Chiappe et Al. acquired STM images showing evidences of flat Si-induced features, figure 1.13(b) and (c). The RHEED pattern before and after the evaporation shows the same streaks ruling out the possibility of a reconstruction at the surface. A model based on DFT calculations was proposed. According to it, silicon atoms arrange themselves in the atomic sites of the last MoS$_2$ layer. The important mismatch between the lattice constants of predicted free-standing silicene (3,8 Å) and the one observed (3,2 Å) is explained in terms of high buckling of the silicon sheet ∼2 Å, figure 1.14. In the same image it is clear that the Si layer is composed of low-lying silicon atoms, 3,3 Åabove the last MoS$_2$ layer, and high-lying ones, 2 Åabove. Moreover, this model explains also the height profile in the inset of figure 1.13(c).
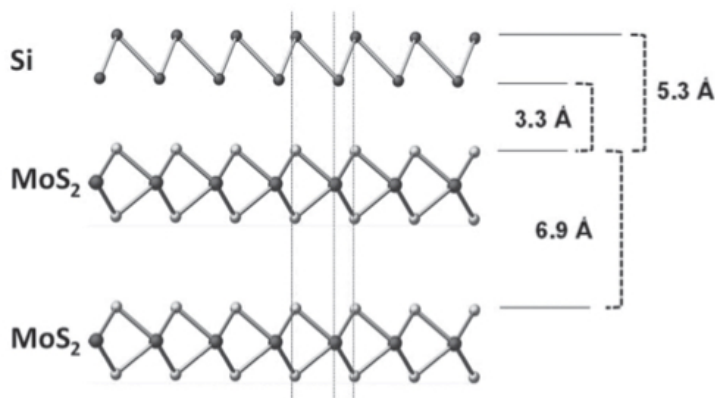
Figure 1.14: High buckled silicene model proposed by Chiappe et al. in order to explain the lattice mismatch between the observed structure and silicene.

Nevertheless, some aspects and conclusions appear to be controversial in this work. First of all, the fact that the RHEED pattern doesn't show any reconstruction could also mean that the silicon deposited at the surface is not arranged in a periodic structure. Moreover, in figure 1.13(b), the silicon induced features appear not very stable: it seems that the scanning movement of the STM tip induces a smearing of the borders of the sheet, which could mean that it tends to drag atoms or molecules, which are not properly fixed or arranged in a static structure. Eventually, the atomically resolved image in figure 1.13(d) cannot be

considered conclusive regarding the ordered arrangement of the silicon atoms, as it is common, during STM measurements, to use tunnelling parameters such that the images acquired show features of the structure underlying the topmost layer.

1.7   Self-assembled nanostructure on HOPG

Another substrate chosen as a possible candidate for silicene growth is Highly Oriented Pyrolitic Graphite (HOPG). Graphite, in general, is a layered structure made of single planar carbon planes, showing an hexagonal pattern, stacked one over the other, figure 1.16. The carbon atoms in the same layer show a trigonal bond, due the overlap of sp_2 hybrid orbitals. Whereas, the overlap of carbon sp_z
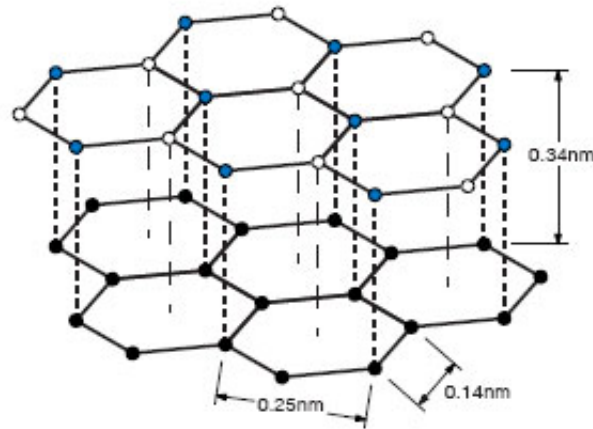
Figure 1.15: Graphite structure: the single planes (graphene) are made of carbon atoms arranged in an hexagonal pattern.

orbitals produces delocalized π-bonds above and below each carbon ring, responsible of the high electrical conductivity. The layers are kept together by weak van der Walls forces. The carbons in the very last layer of an HOPG sample can belong to two inequivalent sites, A and B, indicated by the white and blue dots in the topmost layer in figure 1.16. The presence and the absence of a carbon atom below the two sites determines a higher or lower electron density, respectively, in the sites themselves. This results in the experimental evidence that STM experiments can image only one of the two inequivalent sites depending on the sign of the voltage applied. Cleaving HOPG over the (0001) leaves an atomic smooth and chemically

inert surface with an hexagonal structure, which is why this material seems to be appropriate for silicene growth.

In this paragraph I'd like to discuss some results obtained by Nehzdnanov et al. [26]. STM imaging at room temperature has been used to probe a Si deposit at different thicknesses. It is reported that at ~ 1 ML deposition 2D silicon islands are formed on the HOPG surface. The structure of these features resembles the one of HOPG, figure , included the interatomic distance of $\sim$2,4 Å, corresponding to the distance between two atoms of the same (A or B) site. Further deposition leads to the formation of spherically shaped three dimensional islands.
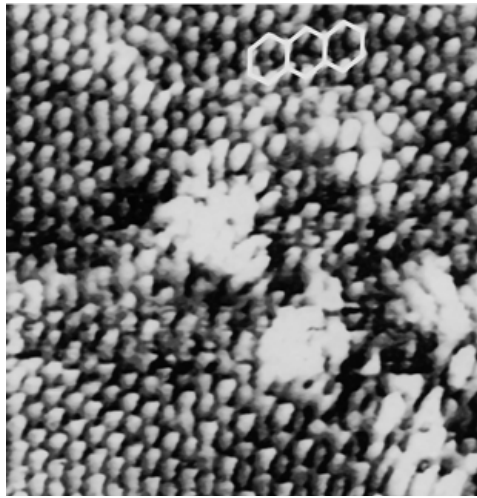

Figure 1.16: STM image (5x5 nm^2) reported by Nehzdanov et al. [26]. The white hexagons highlight the features interpreted as 2D silicon islands.

Chapter 2

Techniques

In this section, after a brief introduction about UHV (Ultra High Vacuum) technology, the main techniques used during the internship shall be presented. In particular, the attention is focused on the physical phenomena exploited and the information one can get from the measurements.

2.1 The UHV technology

In order to ensure the success of the measurements performed, ultra-high-vacuum conditions are needed, which means that inside the preparation and analysis chamber the pressure is kept between 10^{-10} and 10^{-11} mbar. This condition is obtained, maintained and controlled thanks to different pumps (primary, turbo, ion, Ti sublimation) and gauges covering different pressure ranges. Moreover, UHV is required if well-defined surfaces with negligible contamination are needed: at p=10^{-6} mbar, assuming that all the molecules in the ambient stick to the sample, the surface is completely covered in 1 s.

- *Rotary pumps*: they operate in the 10^2-10^{-2} mbar range and are therefore used as primary pumps in order to obtain a preliminary vacuum. The mechanism is based on a rotor which mechanically pushes air molecules out of the chamber, figure 2.1(a) [27].

- *Turbomolecular pumps*: as they works in the 10^{-5}-10^{-11} mbar range they need a backing pump, e.g. a rotary pump. They rely on the action of a high-

speed rotor, whose blades, inclined with respect to the rotation axis, allows to shuffle gas molecules in the backing side where they are expelled by the primary pump, figure 2.1(b) . The efficiency is high for heavy molecules, while it decreases for lighter ones, especially H_2 [27].

- *Ion Pumps*: an electrical discharge is produced between the anode and the cathode. The electrons spiralling in the cell, thanks to an external magnetic field, hit residual gas molecules and ionize them, figure 2.1(c). Thus, the ions are accelerated to the cathode and auxiliary cathode, so that either they are trapped or they sputter Ti atoms from the auxiliary cathode. In the latter case the Ti atoms released settle on the anode helping to trap other gas molecules. These pumps need preliminary vacuum as they operate between 10^{-6}-10^{-12} mbar, or even below.

- *Sublimation Pumps*: a getter material, usually titanium is evaporated from a wire heated by electrical current. The atoms deposit on an inner wall which acts as getter film where gas molecules form stable compounds with a low vapour pressure. Subsequent evaporations renew the film. They are used as auxiliary pumps and are very efficient in pumping active gases [27, 28].

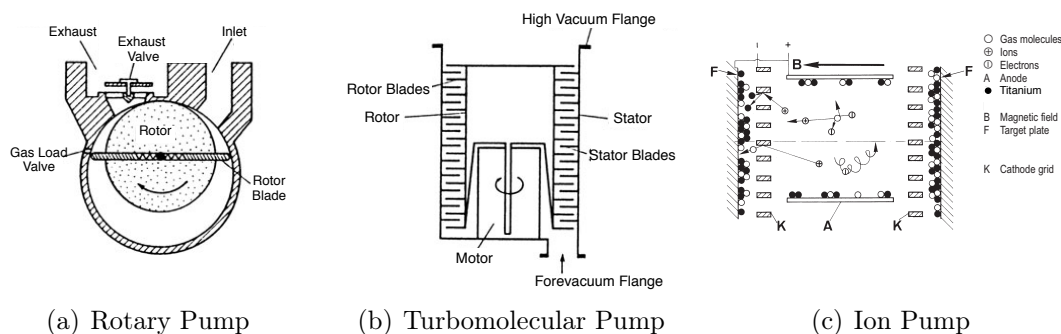(a) Rotary Pump   (b) Turbomolecular Pump   (c) Ion Pump

Figure 2.1: Schematic representation of the main pumps used to get UHV conditions [27, 28]

A fundamental step to obtain UHV conditions is the bake-out of the chamber. H_2O molecules dispersed in air stick to the inner walls of the chamber. Pumping down the chamber they slowly desorb, making difficult to reach pressures below 10^{-8} [27],

despite the pumping power employed. After isolating thermally the apparatus, the temperature is raised up to 170 °C, thanks to resistors or specific heaters. Increasing the temperature, the walls desorb massively the water molecules, which are, then, pumped away.

2.2 STM - Scanning Tunnelling Microscopy

Scanning tunneling microscopy is a technique which allows to study the morphology and local electronic properties of semiconductor and metallic samples with atomic resolution. It was developed by Gerd Binning and Heinrich Rorher in 1981, who received the Nobel Prize in 1986. STM measures the tunnel current between an atomically sharp tip and the surface of the sample, which are kept at a certain bias, as a function of their distance, which can vary between 0.1 and 10 nm [27].
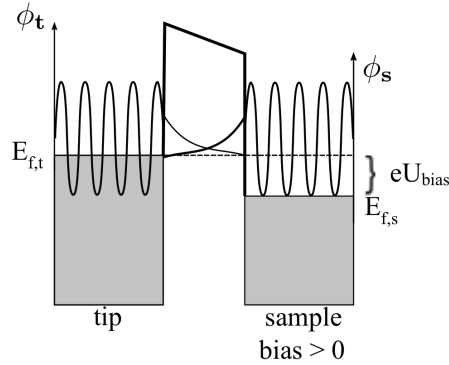

Figure 2.2: Schematic illustration of the tunnelling event occurring between tip and sample, when probing the empty-states of the latter. Shaded parts indicate filled states. eU_{bias} represents the energy shift in the Fermi level of the sample, $E_{F,s}$, which results lowered with respect to that of the tip, $E_{F,t}$. Notice the overlap of the wavefunctions in the barrier.

The apparatus allows tip and surface to be close enough for their wavefunctions to overlap sufficiently, so that electrons can tunnel from one to the other. Applying a bias voltage causes a misalignment of their Fermi levels and depending on the sign of the bias the electrons flow from the tip to the sample (positive bias), probing the empty states of the surface, figure 2.2, or viceversa (negative bias), probing

the filled states. The tunnelling current is given by:

$$i_{tunnel} \propto e^{-2\frac{\sqrt{2m\phi'}}{\hbar}d} \tag{2.1}$$

in which m is the electron mass and d is the distance between sample and tip and ϕ' is a value depending on both the tip and sample work-functions. Practically, only the electrons near the Fermi level contribute to the current. The exponential dependence implies that if d changes by 1 Å, then the current changes by one order of magnitude, which is the physical reason beyond the high resolution of STM. The high accuracy in vertical movements is achieved thanks to voltage-controlled piezoelectric elements, which change their dimensions with a sensitivity as low as $\sim$pm. There are two imaging modes:

- Constant current imaging (CCI): the instant value of the tunnel current is used by a feedback loop (FL), which acts on the tip-surface distance, to keep the interaction at a constant value. All the images were acquired in this mode during the STM session.

- Constant height imaging (CHI): described for sake of completeness, in this mode the distance of the tip is kept constant. The value of the current in each point scanned is used to map the surface.

Being an highly sensitive and sensible technique, isolation from ambient and external vibrations plays a fundamental role in STM. Mechanical vibrations can put in resonance the tip-sample ensemble causing fluctuations of their reciprocal distance, resulting in periodic noise in the images acquired. In order to damp the apparatus, both mechanical, e.g. springs, and eddy current damping system are exploited [29]. The experimental apparatus used here consists in two chambers: the preparation chamber (PREP) and analysis chamber (STM). They can be isolated from one another by closing a valve. Both are pumped with primary turbo and ion pumps; Ti sublimation can be carried out, too. Beside the basic analysis techniques such as AES and LEED, the preparation chamber is embedded with a line for molecular hydrogen, a hot filament, used to dissociate H_2 molecules, and Ta plate, which can be put in contact with a fresh inserted tip in order to flash it. The transfer arm allows to move samples, or tip holders, from the SAS to the

24

manipulator or to the STM chamber. By using the manipulator it is possible to degas the sample. A resistor is heated by direct current and a thermocouple reads the value of the temperature. As the thermocouple is not exactly at the sample position, a calibration was previously done, in order to get from the current applied the right value of T at the sample position. It is possible to connect the sample to electrically opposite poles for direct current heating. This can be useful to prepare certain surfaces or induce reconstructions which require high temperature heating (see next chapter, Si(111)-7x7). The analysis chamber is embedded with a STM Omicron UHV VT XA apparatus. This set-up allows measurements in the temperature range 50-500 K and in-situ observation of the sample during the evaporation [29]. It is interfaced with a computer in which the software MATRIX handles the image acquisition including the setting of the parameters, such as the set current, that is the strength of the interaction, the voltage difference and the loop gain, which determines the sensitivity of the response in the feed-back loop.

2.2.1 Tip Preparation by Chemical Etching

The tips used for the imaging were prepared in the STM room by chemical etching. A schematic drawing of the apparatus is reported in figure 2.3 . The basic idea is to dip the tip, which consists of a simple piece of W wire (purity=99,95%) into the electrolyte solution 2 molar NaOh) so that the circuit in the figure is closed. A current induced by the voltage applied causes the dissolution of the wire. The etching takes place at the air-solution interface, but the reason behind
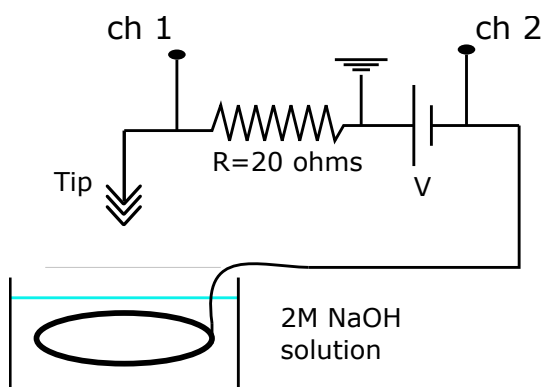

Figure 2.3: Sketch of the apparatus used for the chemical etching of the tip. Ch 1 represents the channel of the oscilloscope used to check the voltage at the extremities of the resistance, thus the current in the circuit. Ch 2 checks the voltage at the exit of the supply.

the final sharp shape of the tip, dwells in the meniscus which forms around the

tip wire when it is immersed [30]. The shape of the meniscus is very important as it results in a slower etching rate at the top of the wire than the one at the bottom. At a certain point the section of the wire at the interface will be small enough, so that the weight of the lower end of the wire will cause a break between the two parts, and a sharp tip will be left in the upper end. This is the so called "drop-off method" and it is represented schematically in figure 2.4 [30]. Once the etching is complete it is mandatory to clean the tip for few seconds in water and afterwards in ethanol in order to stop immediately any residual reaction. The process is monitored through an oscilloscope connected as shown in figure 2.3 : the channel 1 controlled the voltage at the extremities of a known resistance (R=20 Ω), so that one can simply estimate the current in the circuit; the channel 2 keeps controlled the exit voltage of the supply. The voltage supply allows to set a cut-off current. In fact, when the wire breaks the resistance at the tip-solution interface increases steeply and this results in a drop of the current in the circuit. Setting the right value for the cut-off current allows to stop the voltage supply when the break occurs, slowing down considerably the etching process. Tungsten is widely employed in the fabrication of STM as it allows to have sharp tip using relatively mild chemicals. The main drawback is that it is quiet reactive and it undergoes rapidly surface contamination. Nevertheless, in the preparation chamber of the STM a Ta plate can be put in connection with the tip which is flashed, by putting a direct current of ∼4 A.
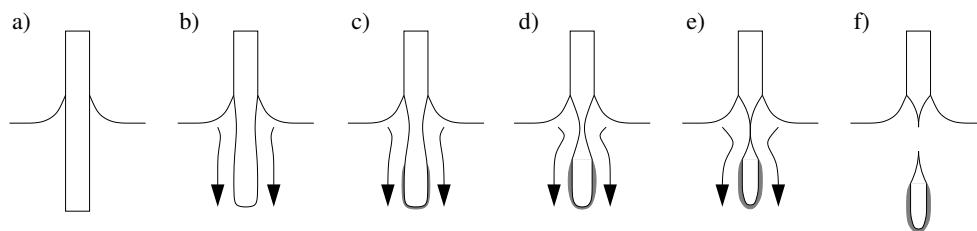

Figure 2.4: Illustration of the "drop-off method". (a) Formation of the meniscus, (b)-(e) appearance of the necking phenomenon at the meniscus, (f) occurrence of the "drop-off".

At temperatures above 1000 °C the tip desorbs the oxide layer (WO$_3$) according

to the following reaction [30]:

$$2WO_3 + W \rightarrow 3WO_2 \uparrow \qquad (2.2)$$

the product of the reaction is volatile and sublimates at 1075 °C. Another advantage is that the annealing process heals defects in the crystallographic structure of the tip, generated during the etching process and the "drop-off", and it can also improve the smoothness of the surface [30].

2.3   AES - Auger Electron Spectroscopy

When an external excitation, e.g. an electron created by an electron gun or X-ray radiation, hits a sample, it can induce the ionization of a core level (K or L shell), generating thus a hole. This core electron leaves the atom with an ill-defined energy, due to the complexity of the scattering process. An electron from a higher-lying shell fills the hole left by the core electron. Two concurring processes can then be observed: the de-excitation can come along either with the emission of characteristic X-ray radiation, or with the radiationless Auger process, figure 2.5 [27, 31].
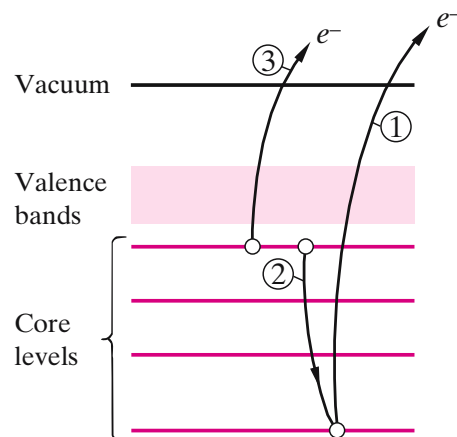
Figure 2.5:   (1) An electron is knocked out of a core level by X-radiation, then another electron fills the hole left (2), releasing enough energy to an external electron to reach the vacuum level.

Concerning the latter, the energy gained during the transition of the electron to the lower-lying core level is exploited to undermine another electron of the atom. In a simple one electron picture the kinetic energy of the Auger electron is equal

to:

$$E_{kin} = E_{L-L} - E_{H-L} - E_{Au} \tag{2.3}$$

in which E_{L-L} is the binding energy of the low-lying level, E_{H-L} is the one of the high-lying one and E_{Au} corresponds to the energy level of the emitted Auger electron. However, the hole created along with the emission of the Auger electron causes a further electronic rearrangement in the atom, which induces a many-electron effect correction in the energy, which should be accounted for [27]. Anyway, the emitted Auger electron carries a kinetic energy which is representative of the energy levels involved in the process, and, thus, it can be used to identify atomic species.

Figure 2.6: (top) Auger signal in terms of count of electrons detected with a certain energy. (bottom) Corresponding derivative-mode signal. Notice that the background is less important in the second case.
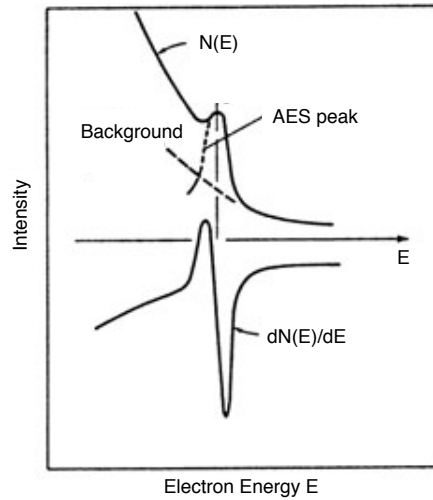
The apparatus consists of an electron gun (E=3000 eV) and a Cylindrical Mirror Analyser (CMA), which selects the energy of the detected electrons. In order to suppress the large background of secondary electrons, which could overwhelm the Auger intensities, AES is carried out in derivative mode, figure 2.6. Practically, a small alternating voltage $v = v_o sin(\omega)t$ is superimposed to the voltage V of the outer cylinder of the CMA. Inthe experiment performed ω= 1 Khz and v_0=0,4 V. A lock-in amplifier detects the in-phase signal, which is proportional to dI/dV [27].

2.4 Spot Profile Analysis - Low Energy Electron Diffraction (SPA-LEED)

It represents a standard technique in surface physics which allows to observe the crystallographic structure of a clean surface as well as of ordered adsorbate overlayers. An electron gun (cathode filament in LaB_6) produces a primary beam (50÷300 eV) which hits the surface. Hereafter, the elastically backscattered electrons give rise to a diffraction pattern. This can be observed either on a fluorescent screen or it can be detected by a channeltron (V=2600 V) interfaced with a computer endowed with a software for the imaging. In the second case, the scanning of the reciprocal space is achieved exploiting octopoles which deflect the primary beam varying the angle of incidence [32].
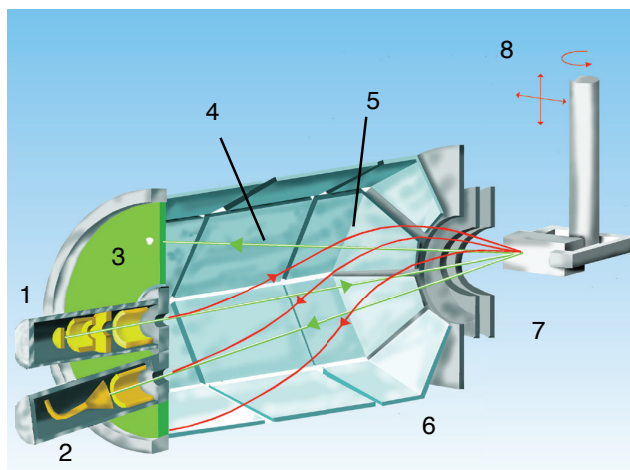

Figure 2.7: Schematic drawing of a SPA-LEED: (1) electron gun; (2) channeltron; (3) fluorescent screen; (4)-(5) electron path in zero magnetic field and in the presence of a magnetic field, respectively; (6) octopoles; (7) entrance lenses for the primary focus; (8) sample holder.

Consequently, each point of the reciprocal space can be focused onto the channeltron in order to map the reciprocal space associated to the sample, figure 2.7 [27]. LEED is sensitive to the very first layers of the sample as it penetrates only few Å in the solid, depending on the energy of the primary beam. The theoretical description is complicated and not trivial because of the strong interaction between low-energy electrons and matter. Anyway within the Kinematic

Theory [27], a qualitative comprehension of the phenomenon can be achieved. Without entering the formalism, the fundamentals approximations of the theory are:

- Single Scattering Events

- Born Approximation

According to this picture the scattering is assumed to occur only in the first atomic layer of the sample, although generally speaking also few layers beneath the first one are involved. This assumption is reflected in the relaxation of the third Laue condition. Only the first few layers are
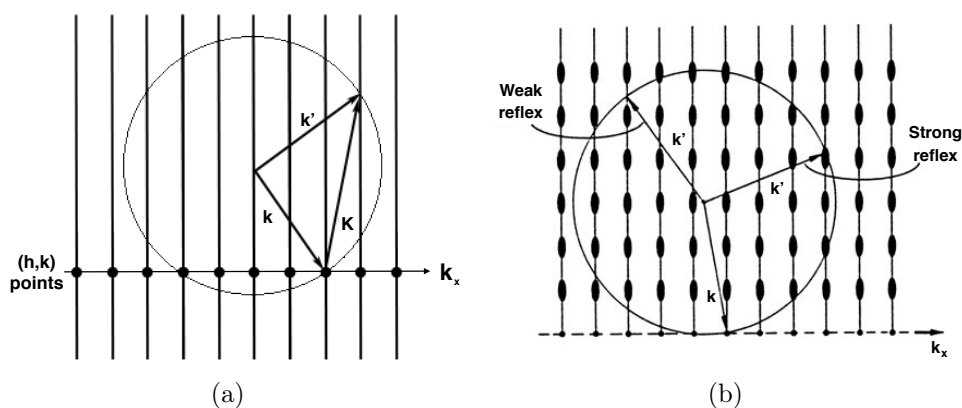

(a)   (b)

Figure 2.8: (a) Construction of the Ewald sphere in the case of scattering from the very first layer of the surface. The reciprocal normal rods reflect the relaxation of the 3rd Laue condition. (b) As the scattering from the planes beneath the very first one become important, the reciprocal rods thickens in the regions where the diffraction points, associated to the bulk structure, should be observed. Note, in general $\mathbf{k}$ is perpendicular to the surface.

Assuming a plane-wave character for the incident and scattered waves, with k-vectors $\mathbf{k}$ and $\mathbf{k}'$, respectively, the 2D Laue conditions write:

$$\mathbf{K} \cdot \mathbf{a} = 2\pi h \quad \mathbf{K} \cdot \mathbf{b} = 2\pi k \quad \text{h,k integer}$$

satisfied when

$$\mathbf{K} = \mathbf{K}_{\parallel} + \mathbf{K}_{\perp} \hat{e}_{\perp} \quad \mathbf{K}_{\parallel} = \mathbf{k}'_{\parallel} - \mathbf{k}_{\parallel} = \mathbf{G}_{\parallel}$$

in which $\mathbf{K} = \mathbf{k}' - \mathbf{k}$, $\mathbf{a}$ and $\mathbf{b}$ are primitive vectors, $\mathbf{G}$ is a reciprocal lattice vector and $\perp$, $\parallel$ refer, respectively, to the perpendicular and parallel components of the vectors with respect to the surface. From a graphical point of view this is obtained by associating to every reciprocal lattice point a rod normal to the surface, figure 2.8(a) . Notice, the condition $\mathbf{K}_\parallel = \mathbf{G}_\parallel$ is fulfilled in each point the Ewald sphere crosses a rod. In real experiments the Bragg rods are modulated by the signal coming from the bulk structure. The intensity of a Bragg spot will be more intense where the Ewald sphere crosses thicker regions of the rod, figure 2.8(b) [27]. It is worth noting that the important cross-section of low-energy electrons results in a strong interaction with the sample probed and causes multiple scattering effects, figure 2.9, which can hamper the interpretation of the diffraction patterns.
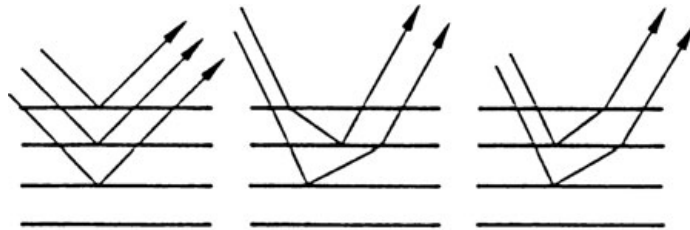

Figure 2.9: Schematic representation of a single scattering process at the lattice planes, which causes regular Bragg reflection (left) and multiple scattering processes, which give misleading contributions to the diffraction pattern (center and right).

2.5 Surface Differential Reflectance Spectroscopy (SDRS) and Thermoreflectance (TR)

This technique is used to study the optical properties (absorption) of solid surfaces, thin films, also during the growth on a substrate. Chemical reactions at the surface occurring during experiments can be observed, too. SDRS exploits linearly polarized light, with wavelength varying from the near UV through the visible to the IR range, which probes the first 10-20 nm of a certain sample. The apparatus used is very simple: it consists in a light source, an optical fibre, which guides both incidence and reflected beam, a light analyser interfaced with a PC and

a software written in LABView, which allows to records the spectra. No vacuum is needed. The light is focused by a lens and shone on the sample, it is reflected and focus again onto the optical fibre. Real time spectra are acquired, so the intensity coming from the UV and visible ranges can be checked. Being the focus point dependent on the wavelength of the light used, it is not possible to focus properly at the same time the UV and the visible light. Thus, a compromise has to be reached in which both signals have a reasonable intensity. Before starting the acquisition the background spectrum, acquired with the light source shut down, is measured and then subtracted from the spectra.

The SDR signal, in the case of evaporation during the measurement, that is the interest of the present work, is:

$$\frac{\Delta R}{R} = \frac{R(d) - R_{sub}}{R_{sub}} \qquad (2.4)$$

where R_{sub} and $R(d)$ are the the optical reflectances of the substrate before evaporation and after the deposition of a layer of thickness d [33]. The utility of this technique lays in the connection between the SDR signal and the dielectric function of the substrate, which is usually known, and the one of the material deposited on its surface. In analogy with the Fresnel equations for a two-phase system, it is possible to derive the counterpart for a three-phase system, that consists, in the present case, in the substrate, the Si layer and the vacuum. These equation, being too complicated to extract easily direct information, are simplified thanks to a linear approximation valid for $\lambda \ll d$ and for an homogeneous film described by a dielectric tensor $\bar{\bar{\varepsilon}}(\omega)$, which leads, in case of normal incidence and light polarization along the x axis, to the result:

$$\frac{\Delta R}{R} = 8\frac{\pi}{\lambda}Im\{\frac{d\varepsilon_{xx}(\omega)}{\varepsilon_{sub}(\omega) - 1}\} \qquad (2.5)$$

where $\varepsilon_{xx}(\omega)$ is the component of the dielectric response tensor of the layer along the x direction, d the thickness of the film and $\varepsilon_{sub}(\omega)$ is the dielectric function of the substrate [15]. If one considers an homogeneous layer with bulk optical response, $\varepsilon_{xx}(\omega)$ can be replaced by $\varepsilon(\omega)$-1, with $\varepsilon(\omega)$ is the dielectric function of the film. Moreover, anticipating Chapter 3, in the case of silver, for an energy

32

of the incident light below 3,7 eV, the real part of the dielectric function of the film is negative and much larger than the imaginary part. Thus, the SDR signal expression reduces to the simple absorption of the film, that is $d\text{Im}[\varepsilon(\omega/)\lambda]$ [15]. Using the same apparatus it is possible to perform also thermoreflectance measurements, whose signal is given by:

$$TR(T) = \frac{R(T + \delta T) - R(T)}{R(T)} \tag{2.6}$$

where T is the temperature of the sample, δT is a small variation of temperature and R(T) is the reflectance at the temperature T. This kind of experiment gives precise information about the position of the optical critical points related to interband transitions, both for metal and semiconductor crystals.

Chapter 3

Experiments and results

In this chapter I will present and discuss the experimental results. Two chambers were mainly used to perform the measurements. The STM apparatus was described in the last section. The other chamber allows Auger and SPA-LEED analysis and argon ion sputtering. In this chamber AES can be performed during Si evaporation keeping the sample at 45° between evaporator and Auger set-up, so that growth can be followed in situ. The evaporation of silicon is obtained by sublimation from a wafer crossed by direct current. SDRS study on Ag(111) was performed in this very chamber, too. Also in this case the evolution of the optical response of the sample was followed during Si evaporation. In this configuration the evaporation is at ∼90° of incidence and also the SDRS is performed at normal incidence. The main characteristic of the LEED apparatus have been given in the last section.

The substrates have been chosen taking into account different aspects. The main guideline has been the literature published in the last years. Both theoretical predictions and experimental observations have been useful to make a guess of what one could expect from the deposition on a certain substrate. Moreover, from a practical point of view, the constraints which are mandatory to consider, concern the expected symmetry of silicene and the unit cell dimension. An important mismatch in the lattice constants would result in a considerable strain at the interface which could prevent the superstructure from forming. Moreover, some substrates need particular preparations which could demand a controlled environment or the

use of dangerous substances. For example, the hydrogenation of Si(111) can be obtained exploiting aqueous etching by HF acid, which is extremely toxic and it has to be handle with great care. In the present case a direct exposure to atomic H in UHV has been preferred to hydrogenate Si(111) surface, as it will be shown.

3.1 Ag(111)

In this part I briefly describe the results obtained for thick Si deposits on Ag(111) kept at high temperature ($\gtrsim$200 °C). The aim of the study is to understand the origin of the $\sqrt{3}$x$\sqrt{3}$ reconstruction.
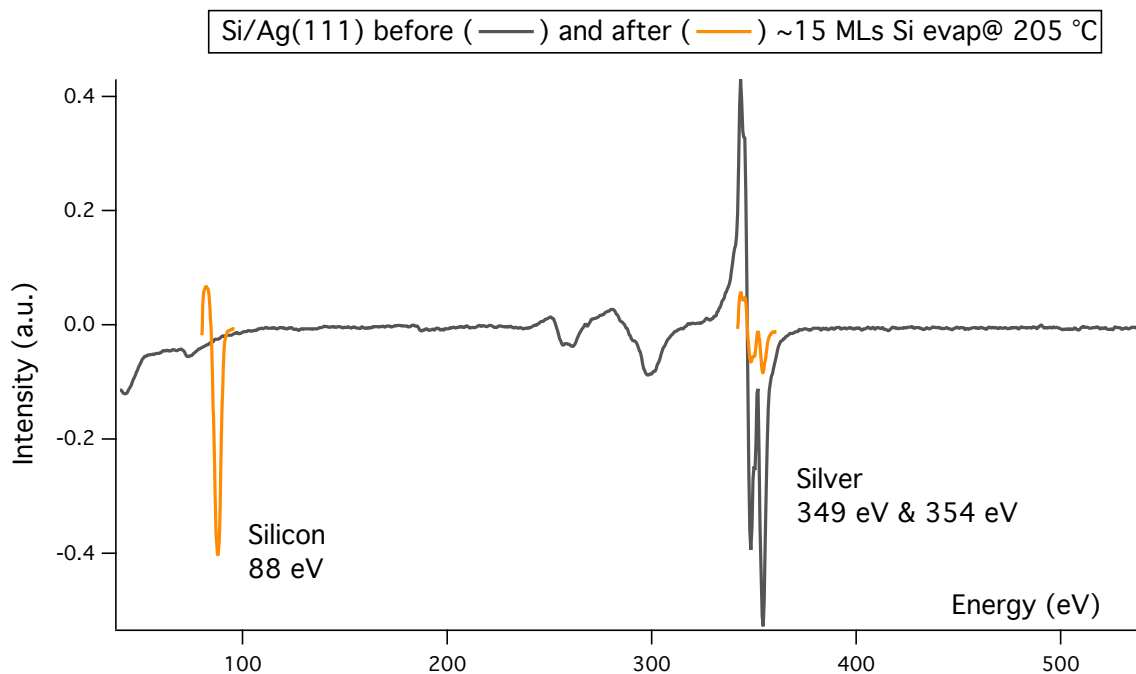
Figure 3.1: AES spectrum taken at 45° incidence in differential mode (see chapter 2). The grey curve represents the bare Ag(111) substrates at room temperature, while the orange peaks are how the Auger signal looks like after 15 MLs of Si deposition in the ranges 70-90 eV and 340-360 eV. The peaks have been identified comparing qualitatively their position with the references known from the literature [36].

It is worth to spend few more words about the issue of silicon growth onto

Ag(111), introduced in chapter 2. It has been reported in several articles that silicon forms stable 2D arrangements onto silver. Moreover depending on the temperature of the substrate and the coverage, different configurations of the silicon atoms can be observed [20, 21], as in figure 3.2 [18] for example.
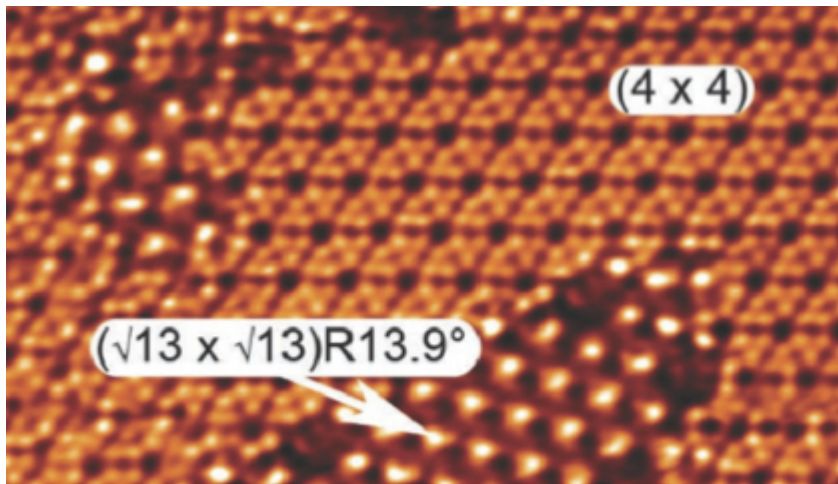

Figure 3.2: Atomically resolved STM topography 18x10 nm^2 with two reconstructions labelled in the picture.

Unfortunately, the characterisation of the electronic properties of these interesting reconstructions have showed that their presumed silicene nature is spoiled by the strong coupling between the substrate and the silicon over-layers. In order to remedy to this problem, it is possible to grow thicker Si deposit onto Ag(111) so to have several layers of silicon/silicene. In this case it is expected that the very first layers of silicon grown onto Ag(111) will still interact strongly with the silver substrate, but on the other hand it is conceivable to think that the last layers deposited will not couple with Ag, being few nanometers distant, so that they would show more likely a silicene nature. Now when a thick silicon deposit is evaporated onto a silver substrate, an unexpected reconstruction is observed [22, 23]: the $\sqrt{3}$x$\sqrt{3}$, figure 3.3 [23].

What makes it unexpected is that it has been observed only for long Si evaporation onto silver and, moreover, bulk-like silicon does not reconstruct in this arrangement. In a first moment, these considerations has made the researchers think about a new 2D arrangement of silicon, but further investigations [22] have
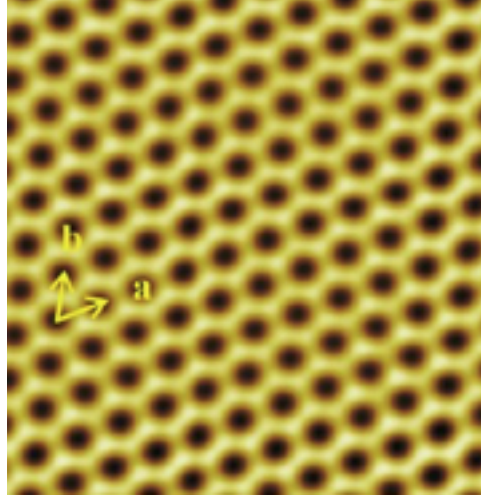
Figure 3.3: One monolayer silicene terrace showing the $\sqrt{3}$x$\sqrt{3}$ honeycomb reconstruction with the period of 0,64 nm.

pointed out that some properties of the systems showing this reconstruction are much more similar to Si(111) $\sqrt{3}$ x $\sqrt{3}$-Ag. So the concurring hypothesis to multilayer silicene is that the deposit is bulk-like silicon and that there is a surfactant effect of the Ag atoms which migrate towards the surface during the evaporation and in the end segregate in proximity of the surface giving rise to the reconstruction observed. Thus, in order to shed some light onto this aspect several techniques have been used:

- Auger Electron Spectroscopy: to check the chemical composition of the surface;

- Low-energy Electron Diffraction: to confirm the presence of the $\sqrt{3}$ x $\sqrt{3}$ reconstruction;

- Surface Differential Reflectance Spectroscopy and Thermoreflectance: to compare the optical response of the system with the ones predicted for bulk-silicon, silicene and silicite (multi-layer silicene).

We now turn the attention to the experiments and the results. First of all, due to its reactivity with atmospheric gases, Ag(111) surface needs to be prepared with great care. In order to do that, cycles of ion argon sputtering (7,5 10^{-5} mbar) and

38

annealing (T~550 °C, 10 min) were performed until Auger spectroscopy gave no sign of impurities due to air exposure, figure 3.1, and a sharp hexagonal pattern was observed by LEED measurements.
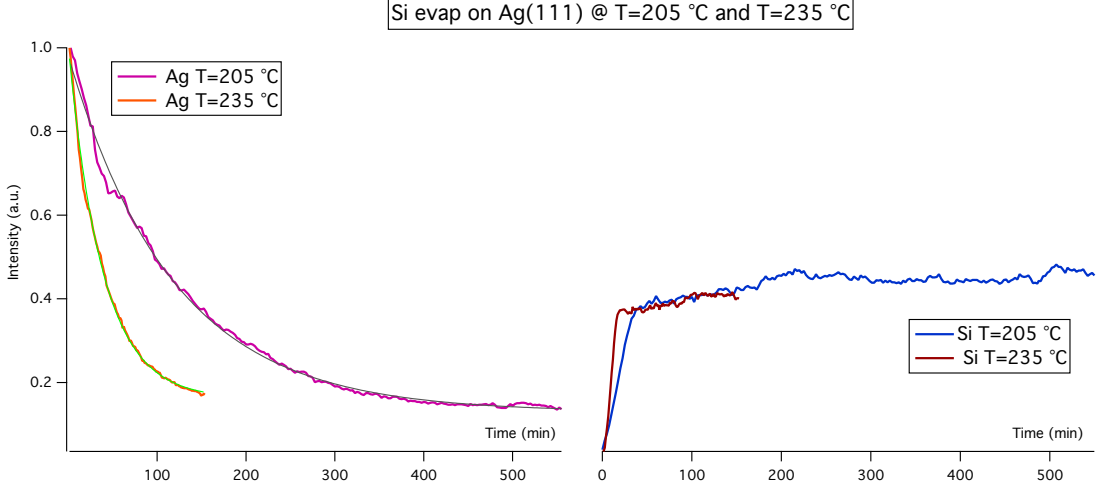

Figure 3.4: Auger signal of the Ag and Si peaks during evaporation as a function of time at 205 °C and 235 °C. In detail, the intensity difference between the positive and negative peak of Si (Ag), figure 3.1, as a function of time, that is coverage.

Si evaporation (I_{wafer}=15,5 A, evaporation angle 45°) at T=235 °C and at T=205 °C on a clean Ag(111) substrate, were followed by AES measurements. In figure 3.4 the normalized Auger peak-to-peak intensity is reported as a function of the time during Si evaporation. It can be seen immediately that the signal of silver, in both cases, decreases exponentially to a value different from zero, y_0^{235}=(0,162 ± 0,002) a.u. and y_0^{205C}=(0,1297 ± 0,0017) a.u. . If there was no interaction between Si and Ag, one would expect the silicon to grow, along with its signal, covering more and more the surface, until the electrons of the primary beam could not reach the substrate. This would result in the complete suppression of the Ag signal. As this is not the case, it can be argued that silver atoms migrate from the substrate to the silicon surface (surfactant effect) where they can still be detected. This consideration agrees with the conclusion presented by Shirai et al. [22]. The curves in figure 3.4 have been fitted with exponential functions:

$$exp(t) = y_0 + A\ exp(-invTau\ t) \tag{3.1}$$

39

Temperatures	y0 (a.u.)	A (a.u.)	invTau (1/min)
205 °C	0.1297±0.0017	0.850±0.004	0.00847±8 10^{-5}
235 °C	0.162±0.0092	0.841±0.004	0.0262 ± 0.0003

Table 3.1: Parameters obtained from the exponential fit of the Ag AES signals in figure 3.4.

where invTau is the inverse of a time constant (1/min), t is the time in minutes, y_0 is the saturation value and A the amplitude of the exponential. The results of the fit are listed in Table 3.2.

It can be argued that the discrepancy between the two saturation values relates to the different temperatures. A higher temperature can favour the migration of silver atoms towards the surface, i.e. it enhances the surfactant effect. From the two values of y_0 it is possible to estimate the quantity of silver at the surface: Q_{Ag}^{235}=(0,347±0,004) ML and Q_{Ag}^{205}=(0,278±0,004) ML, see Appendix.

Si 1× 1

Silicene $\sqrt{3} \times \sqrt{3}$
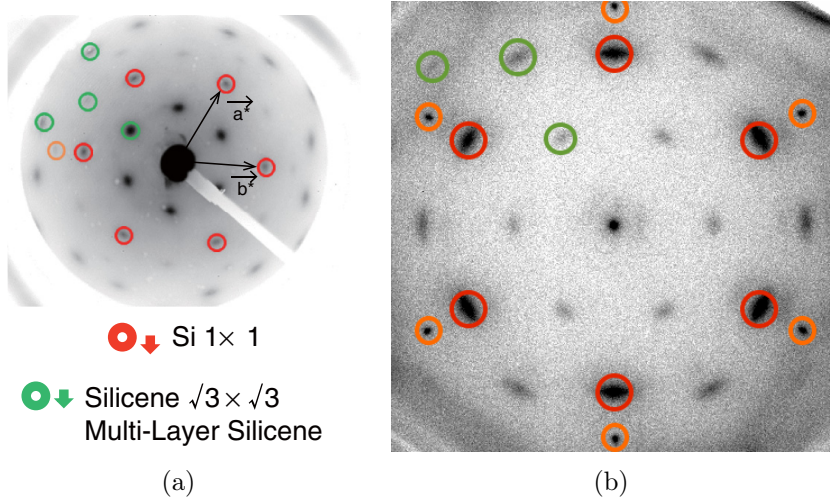Multi-Layer Silicene

(a)   (b)

Figure 3.5: (a) LEED pattern obtained by Shirai et al. [22] (b) LEED measured after the Si evaporation relative to figure 3.4 (400x400, I_{fil}=1,3 A, 8 ms/pt). Comparing the two, it is evident they show the same pattern. The orange circles refer to Ag.

The electrons of the primary beam probing the Si and Ag energy ranges have different energies resulting in different mean free paths, i.e. different depths of penetration. Evidently, this is the reason why in both cases the steep increase in

the silicon signal stops suddenly while the silver intensity preserves its exponential trend: the electrons probing the silicon range have a penetration depth too short to reach the silver substrate, that is the signal has almost the same intensity as for bulk silicon. Note that despite the higher temperature, at T=235°C the silicon covers more quickly the surface. As the wafer broke right after the measurement, this strange behaviour is explained in terms of higher evaporation rate due to the thinning of the silicon wafer: the thinner the wafer the higher the resistivity, the heat dissipated and the evaporation rate.

Of course a similar result could be expected in the case of Volmer-Weber growth, but the literature [20–22, 24] reports that under the conditions used, a layer-by-layer growth is expected. Moreover, also the LEED acquired after the evaporation, figure 3.5(b), shows the same features observed by Shirai et al. [22].

3.1.1 SDRS and thermoreflectance (TR) measurements on thick deposit of silicon onto Ag(111) at 200 °C

The results presented so far hamper the hypothesis according to which the silicon layers grown have a silicene nature, and attribute the $\sqrt{3}x\sqrt{3}$ reconstruction at the Ag atoms migrated to the surface, not to silicon. In order to further confirm this statement, SDRS and TR have been performed on Ag(111) during silicon evaporation.

We start by observing that the band structure for silicon bulk, figure 3.6, shows four direct inter-band transitions which result in as many peaks in the reflectance, figure 3.7(b). In figure 3.7(a) it is possible to observe the evolution of the intensity of the SDRS signal at 3,6 eV and 3,9 eV. A change in the slope is evident at 2800 s, which should correspond to the first monolayer deposition. Assuming that the first layer is silicene, its thickness is expected to be 0,314 nm. If the sticking coefficient does not change, after 18800 s I have grown 2,1 nm, which correspond to 6,7 MLs of Si (either bulk diamond-like or silicite, that is the hypothetical layered allotrope of silicon).

We mainly focus on the direct transitions of bulk silicon at 3,4 eV (E_0', E_1) and at 4,5 eV (E_2) and, in particular, on their corresponding peaks in the Si reflectance spectrum, figure 3.7(b). Silver has reflectance almost equal to one and
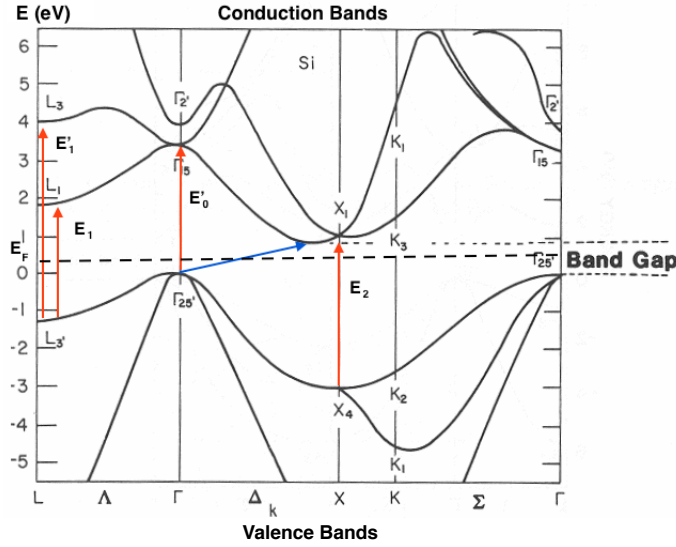
Figure 3.6: Band structure of bulk-silicon. The red arrows represent direct inter-band transitions the blue one is the indirect one. E_F labels the Fermi level.

then suddenly drops close to zero due to the plasmonic resonance frequency. This can be observed in figure 3.7(c) along with the change due to silicon deposition.

In figure 3.7(d) is finally presented the SDRS spectrum obtained at the end of evaporation and at 3 MLs coverage. Qualitatively, the effect of the E_0/E_1' Si transition peak is reflected in the negative shoulder at 3,3 eV. The temperature is expected to broaden the transition peaks and to shift them to lower energies, which can be slightly observed comparing figure 3.7(b) and 3.7(d). Anyway, 6,7 MLs Si deposition on Ag(111) should not have the same optical response of bulk silicon. In fact, it is reasonable to think that very last layers near the surface and the ones closest to the Ag/Si interface have a different optical response. This is expected to damp the negative shoulder at 3,3 eV of bulk silicon in the actual sample. This is confirmed by the fact that the feature is almost not present in the 3 MLs curve in figure 3.7(d), showing that for such thickness the silicon film does not have the bulk Si electronic and optical properties.

Once the deposition is finished, it is possible to study the differential reflectance while changing the temperature (thermoreflectance measurement). In figure 3.8 (top), the reflectance of silicon as a function of the temperature is presented. It can be seen that an increase of temperature results in the broadening and shift to lower
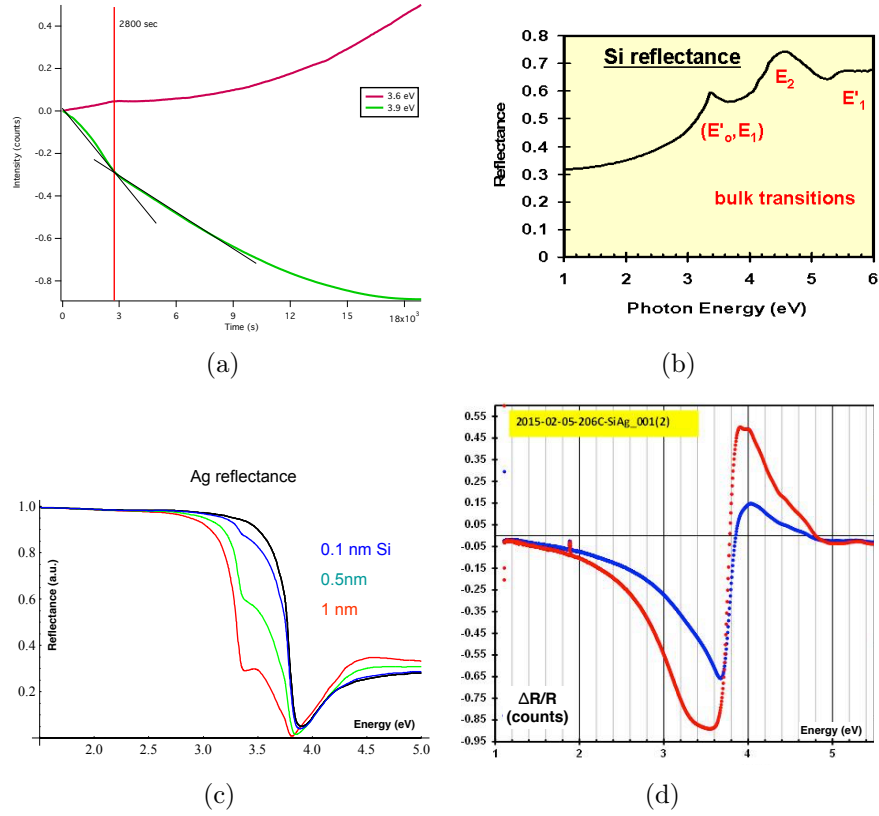
Figure 3.7: (a) Time evolution of the SDRS intensity at 3,6 eV and 3,9 eV, for which the change in the slope is more evident. (b) Silicon reflectance and labelled bulk transitions. (c) Ag reflectance and its evolution for different silicon coverages. (d) SDRS signal after 6,7 (red) and 3 MLs deposition (blue).

energies of the two peaks associated to the interband transitions of bulk Si. These effects are the reason behind the derivative-like features at 3,35 eV and 4,3 eV in the thermoreflectance spectra in figure 3.8 (bottom). TR measurements performed the last November on Si and Ag show a good agreement with the predicted TR spectra. In figure 3.9 it is presented the TR measurements obtained from our sample and it is compared to the TR spectra obtained for silicon and silver last November. Beside the features at 3,35 eV and 4,3 eV due to bulk silicon, another feature is observed at 3,75 eV, which is caused by the Ag substrate probed by light across the Si film grown on it. Thus, the results can be explained considering that the silicon film grown onto Ag(111) substrate has the diamond-like bulk structure.
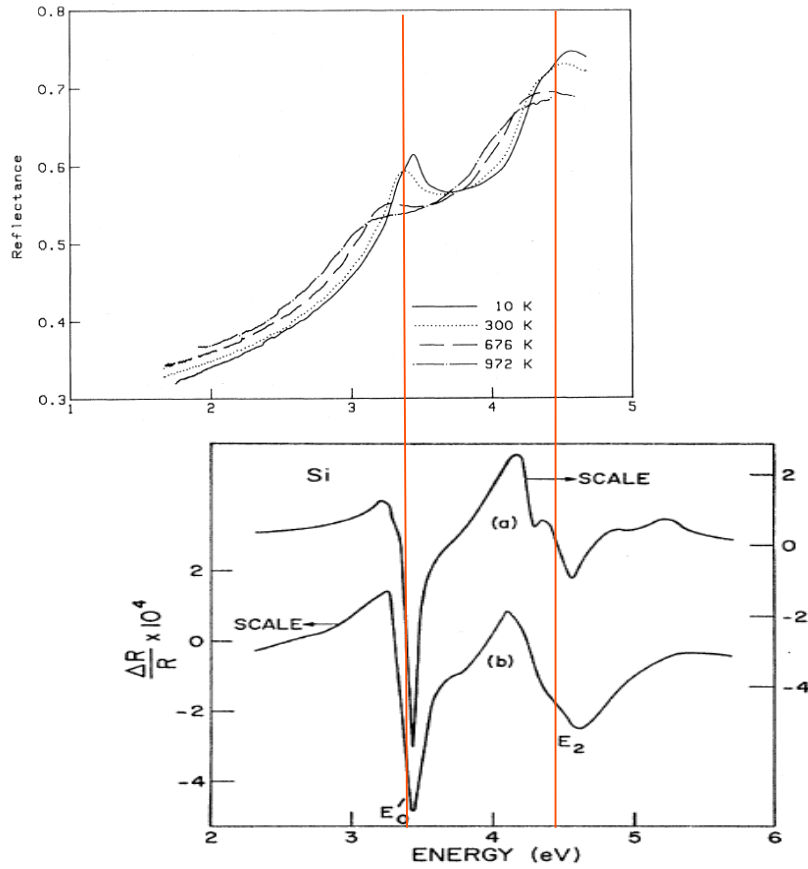
Figure 3.8: (Top) Normal incidence reflectance at different temperatures [34]. (Bottom) TR spectrum at liquid N_2 temperature (a) and at RT (b) [35].

This rules out the hypothesis of multilayer silicene, agreeing with what it has been observed with AES and LEED.

It has been said that the optical response of the deposited silicon differs from the one expected for diamond-like bulk silicon, because near the Si/Ag interface and close to the surface the optical properties are different. Moreover AES measurements have shown a migration of Ag atoms towards the surface. Thus, in order to make clear the contribution to the optical response of Ag atoms observed at the surface of deposited silicon, it would be interesting perform SDRS and TR onto Si(111) with thin silver deposit, and then compare the results to the experiments already done.
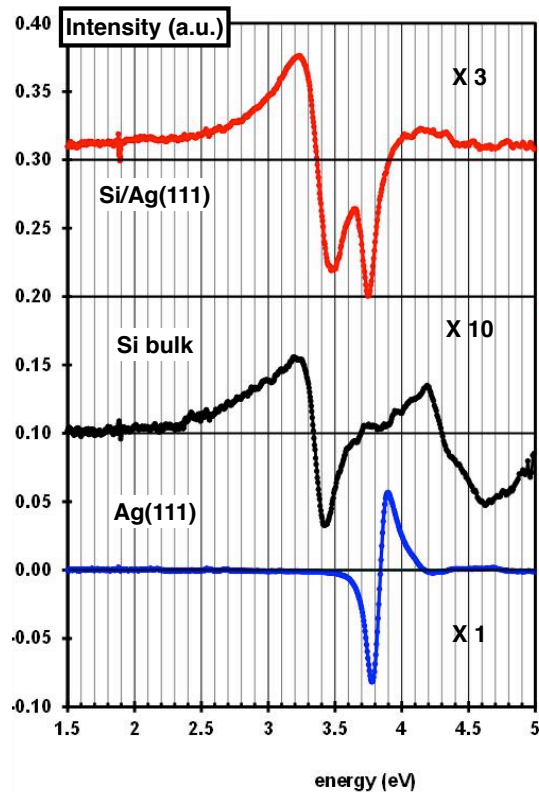
Figure 3.9: (Top) TR mesurements ($\Delta T \approx 50$ °C-75 °C) after evaporation of Si onto Ag(111). (Middle) TR measurement for bulk silicon ($\Delta T \sim 20$-22 °C). (Bottom) TR measurement for Ag(111) ($\Delta T \sim 40$-60 °C).

3.2 Highly Ordered Pyrolitic Graphite - HOPG

STM imaging along with AES measurements have been performed during this internship, in order to investigate silicon deposition onto HOPG and check if silicene-like structures can be observed. The HOPG samples were cleaved in air and degassed in situ at T$\sim$100 °C, using a filament on the manipulator. The bare substrate was observed by STM: the distance between two consecutive protrusions is 0,29 $\pm$ 0,01 nm. Note that this is the distance between the second neighbour atoms in one carbon layer, as it is well known from the literature [38]. First neighbour atoms belong to two inequivalent atomic sites, as one is superimposed to an atomic site of the underlying layer (A atoms) and the other is not (B atoms). Carbon atoms in B sites show a higher local density of states (LDOS) due to the fact that they do not overlap with atoms in the second layer. Note that because of a bad calibration of the piezo the vertical distances are overestimated of a factor of 1,19 and horizontal distances are overestimated of 1,1 factor. Thus, the final result
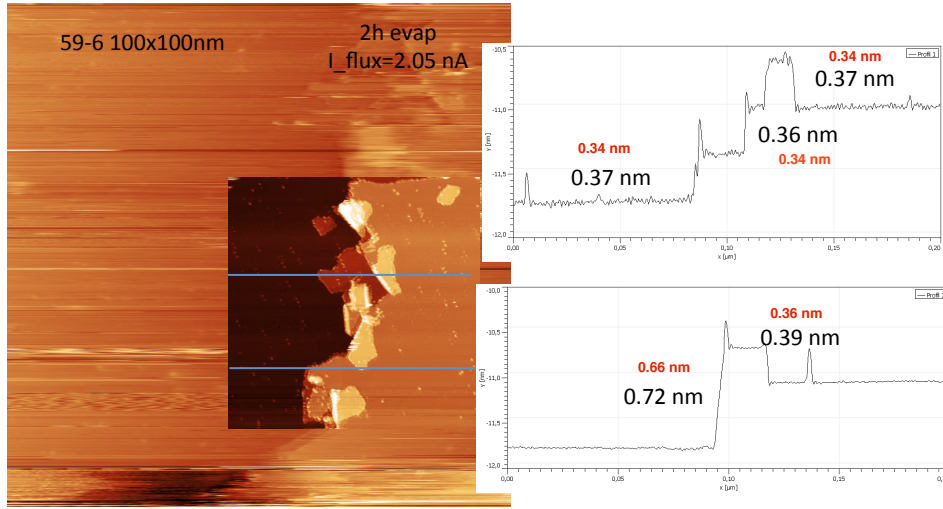
45

Figure 3.10: STM images (100x100 nm^2 and 50x50 nm^2, I$_{set}$=50 pA, V$_{bias}$=0,2 V) showing a step edge and some flat features. Unfortunately, the tips were often unstable, as it can be seen from the image. The profiles are relative to the blue lines. The red values take into account the overestimation factor of 1,1.

for C-C distance is 0,244 ± 0,01 nm, in good agreement with the literature [38].

After performing Si evaporation (I$_{flux}$ =0,85 nA, 1h30min) onto HOPG at RT the first features on which the attention was focused were islands ∼4 nm large and ∼0,4 Å high. Their nature has not been determined yet, but comparing the images before and after evaporation is clear they were induced by silicon evaporation. In some pictures, figure 3.10, some flat features were noticed after deposition, but in all the cases studied the step height measured was suspiciously close to the one expected for graphite (3,4 Å). Some reconstructions of the surface near step edges and other defects were observed, but from comparison with the literature [37], they have been identified as the ($\sqrt{3}$x$\sqrt{3}$)R30° reconstruction. I performed Si evaporation with HOPG cooled down with liquid nitrogen (T=102 K). Interesting islands, 3 nm high, are clearly visible in figure 3.11. They show corrugation on the top, but due to the instability of the tip the morphology does not appear clearly. This observation is bizarre as one would expect to observe a wetting of the surface, as at such a low temperature the atoms deposited on the surface have a short diffusion length. In figure 3.12 is presented the evolution of the intensities of the peaks relative to carbon and silicon, during evaporation of the latter on
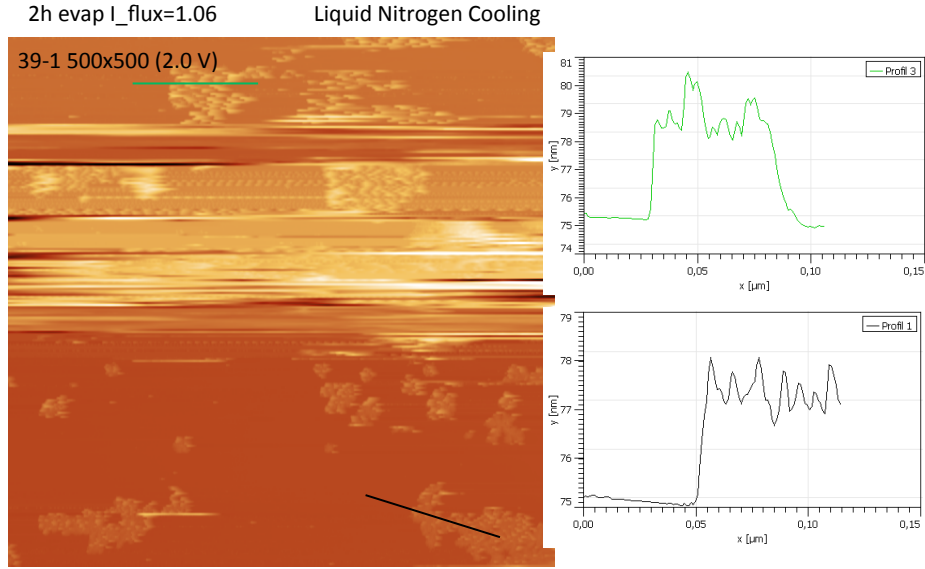
Figure 3.11: STM image (500x500 nm^2, I$_{set}$=30 pA, V$_{bias}$=1,7 V), with islands induced by silicon evaporation and their height profile.

the HOPG substrate at RT. In this case too the signal of the substrate doesn't go to zero. Combining this information with the observation of islands after silicon evaporation, it can be argued that the signal is representative of a 3D growth. This is also in agreement with the increased temperature, which eases this kind of growth.

3.3 Si(111)1x1-H

Among the experiments performed, silicon evaporation on hydrogenated Si(111) has been the most difficult, concerning especially the sample preparation. After the degassing of the sample, the first step was obtaining a sharp Si(7x7) reconstruction. After repeated attempts, it has been noted that the best surface is obtained after three flashes of the sample at ~1000 °C, each time decreasing slowly the temperature around 800 °C, at which the 7x7 transition occurs [38]. The sample was heated by direct current and the temperature was checked with a pyrometer. Concerning the hydrogenation, molecular hydrogen was introduced in the chamber and hot tungsten filament (~ 1800 °C), placed in front of the sample, was used
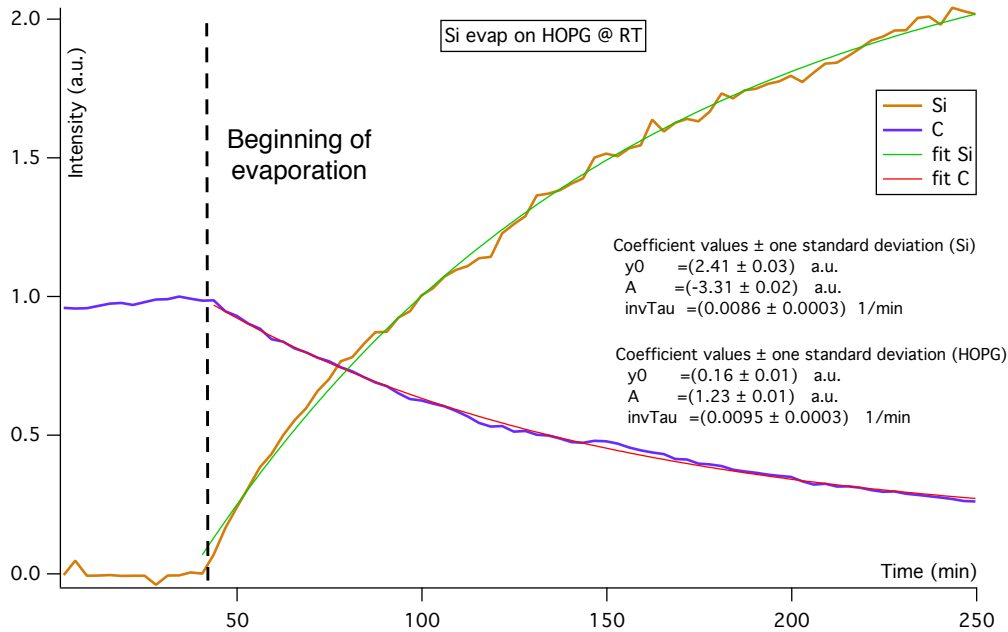
Figure 3.12: Auger signals of C and Si during silicon evaporation (I_{wafer}=15,5 A) at RT and relative fit.

to dissociate it. The temperature of the substrate was decreased before stopping the hydrogenation, reducing the amount of H atoms leaving the surface. From the literature [39], the surface with less defects can obtained for 5000 L (1 Langmuir= 10^{-6} torr·s), but in the present case the best hydrogenation was obtained for 500 L. It is worth noting that what is measured is the exposure of the sample to H_2 and not the effective amount of H atoms reaching the surface, which can depend on other factors, such as the relative position of sample, filament and H_2 line. Considering the dimer adatom stacking fault (DAS) model [38] for the description of the 7x7 reconstruction, the hydrogenation is composed of two steps:

- removal of the adatoms and saturation of the dangling bonds left by H atoms;

- for higher exposures the dimers present at the borders of the 7x7 unit cell break, leaving a 1x1 reconstruction.

Looking at the STM images in figure 3.13(c) is evident that only the first step occurred, as the borders of the 7x7 unit cell are clearly evident. According to this
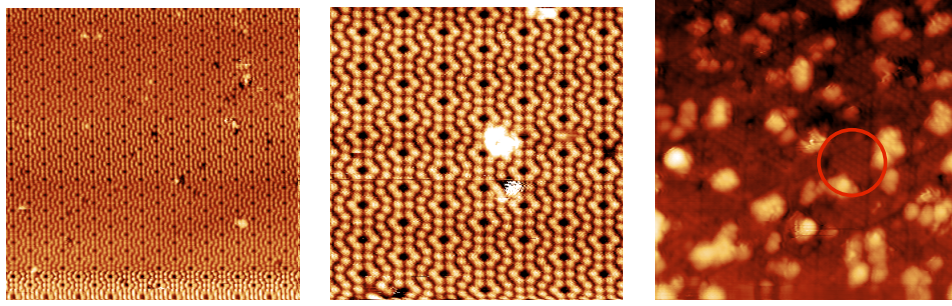
Figure 3.13: STM images (I_{set}=0,1 nA, V_{bias}=2 V) of the 7x7 reconstruction. Left: 50x50 nm^2; center: 20x20 nm^2. In the right image (I_{set}=0,32 nA, V_{bias}=1,7 V) it is shown the surface after 500 L exposure

observation larger exposures have been tried, but the surfaces afterwards showed a high density of defects, which discouraged any attempt of silicon evaporation. Only in one case Si deposition has been performed. In order to observe the silicon growth in situ, two spots separated by ∼2 nm were chosen, poor in defects, but with step edges easy to identify. In figures 3.14(a) and 3.14(b) the same spot before and after evaporation is shown: unfortunately the substrate before deposition did not show a clear 1x1 reconstruction; in this conditions the silicon, after 2 hours evaporation arranges itself in a completely disordered manner.
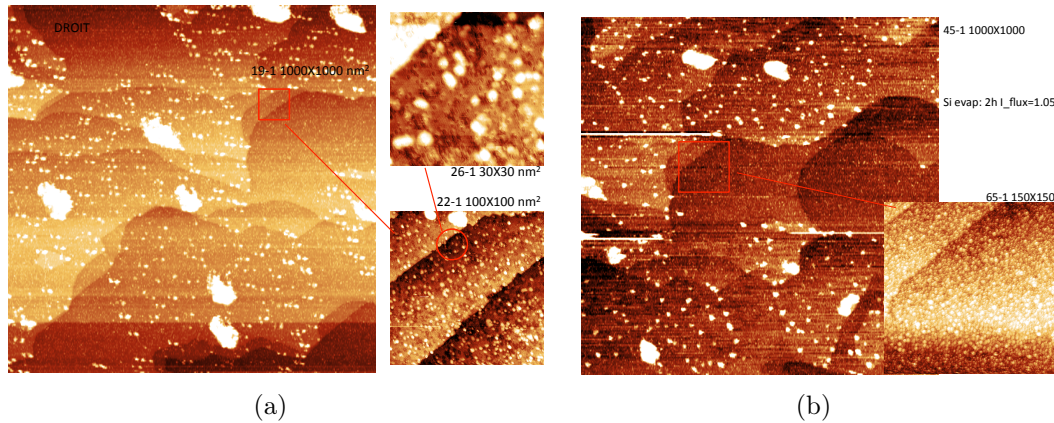

(a)   (b)

Figure 3.14: Large scale STM images and zooms of Si(111) before (a) and after (b) silicon evaporation. (a) I_{set}=0,3 nA, V_{bias}=1,5 V; (b) I_{set}=0,2 nA, V_{bias}=0,2 V

49

3.4 MoS$_2$

In the first chapter a brief discussion has been reported about a recent article [25] in which it is claimed that silicene-like structures have been observed after Si deposition onto a MoS$_2$ substrate. STM observations during silicon evaporation at RT, LEED and AES measurements have been performed in order to shed some light on this subject.
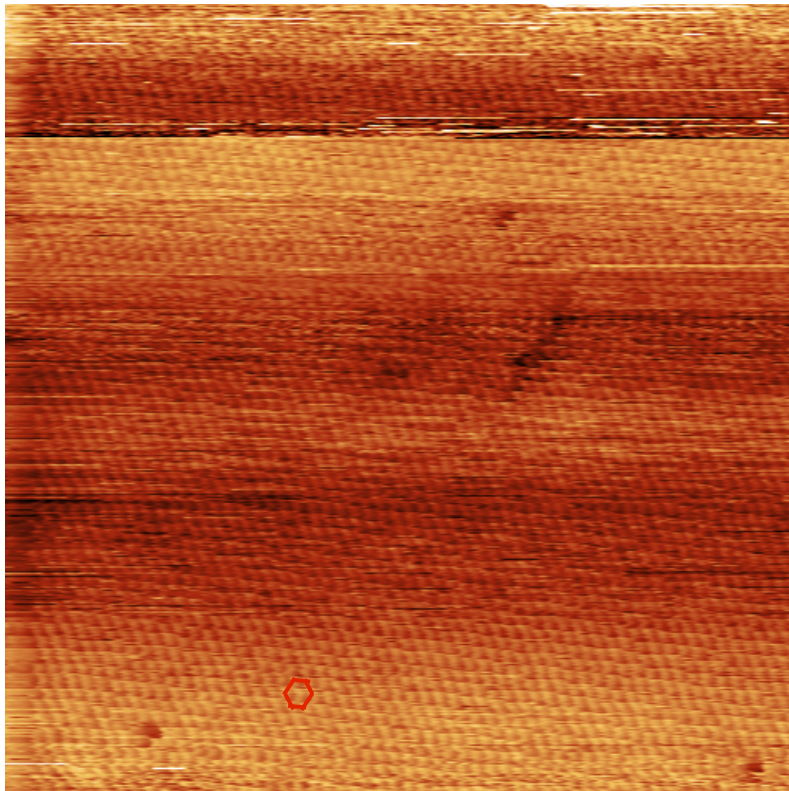

Figure 3.15: STM image 20x20 nm^2 (parameters V$_{bias}$ =-1,5 V, I$_{set}$=0,05 nA) of the bare MoS$_2$ substrate.

The samples were cleaved and fixed on a plate with tantalum stripes and they were degassed at T=400 °C during the night. Concerning the STM session it was noted, according to the literature [40], that the imaging of the bare substrate is easier at negative bias. Anyway, the situation changed a lot after silicon deposition and the imaging was very sensitive to the parameters of acquisition. Often the instability and the shape of the tip hindered the interpretation of the images.
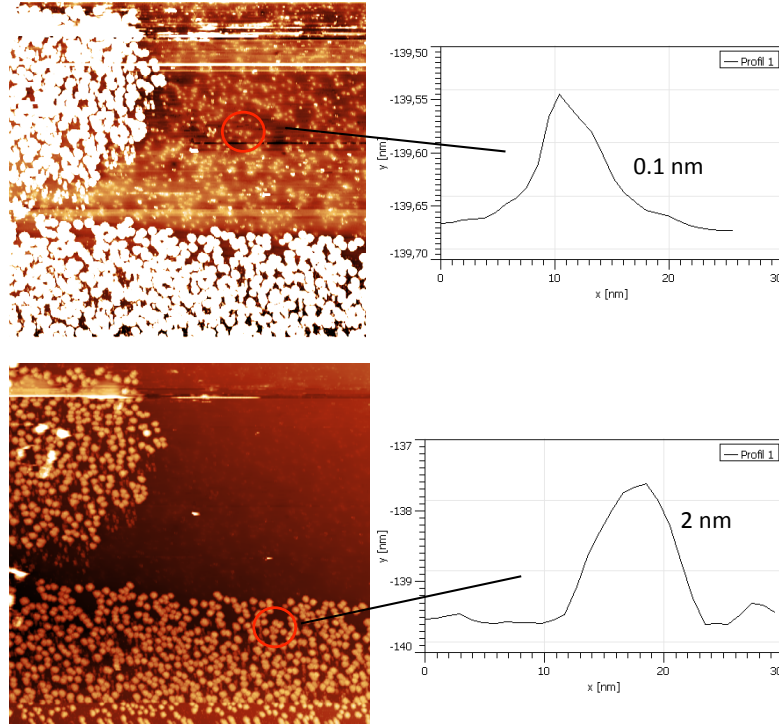
Figure 3.16: Same STM image 500x500 nm^2 (parameters V$_{bias}$ =-1,5 V, I$_{set}$=0,05 nA with different contrast to highlight two kinds of islands.

In figure 3.16 it is possible to observe two kinds of islands observed after silicon evaporation (30 min I$_{flux}$=0.92 nA). Note that the features observed are affected by the shape of the tip. The way in which the defects of ∼2 nm are arranged suggests that this area had been already scanned before and probably the tip could have induced a displacement of the islands. It is worth noting that the bigger islands shows the same height of the one observed on HOPG; unfortunately nothing can be said about the morphology in this case. A 5 nm high defect can be observed in figure 3.17 (top). Small scale images of it were acquired in order to observe an atomically resolved structure, without success. The most interesting observation is shown in figure 3.17 (bottom), in which a feature very similar to the one commented by Chiappe et al. [25], see paragraph 1.6, can be seen. In the present case it was not possible to acquire atomically resolved images of these structure. Evidently, the movement of the tip affects the morphology of the feature as it can be deduced by the smears along some scanning lines, as it was pointed

51

out also in the case taken from the literature. Moreover it was claimed that these silicon induced structures were due to a high-buckled (2 Å) Si arrangement at 0,3Å above the MoS_2 substrate. Surprisingly, the line profile obtained, figure 3.17 (bottom), shows only a single step of about 3 Å. This observation raises doubts about the high-buckled silicene model proposed.

AES and LEED experiments were performed at four different temperatures: -144 °C, RT, 200 °C and 300 °C. The AES spectra obtained during silicon evaporation are presented in figure 3.18(a) and 3.18(b), and parameters of the exponential fit are reported in Table 3.2. The silicon wafer for the evaporation was changed just before performing these measurements.
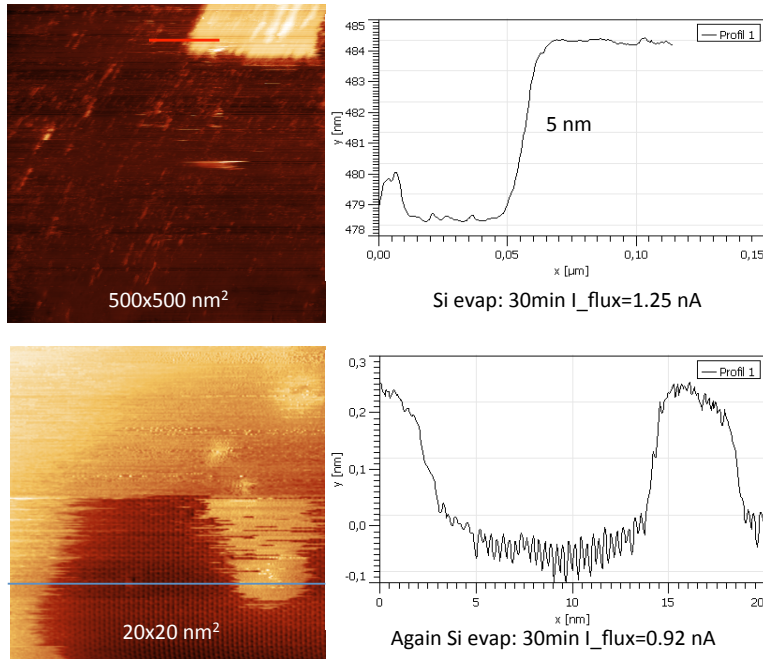
Figure 3.17: STM images 500x500 nm^2 and 20x20 nm^2(parameters V_{bias} =-1,5 V, I_{set}=0,05 nA, RT) and height profiles of the features observed in them.

At T=-144 °C the silver signal of the substrate goes to zero, that is what one would expect from a layer-by-layer growth. At high temperature T=300 °C, on the contrary, the saturation value is different from zero. Taking into consideration the islands observed in figure 3.16, it is reasonable to deduce that the AES signal is representative of a 3D growth. Note that the signals appear very noisy and

| Temperatures	y0 (a.u.)	A (a.u.)	invTau (1/min)
T_{amb}	\\	1.1255±0.0585	0.0055±0.0005
300 °C	0.114±0.009	0.927±0.009	0.0133 ± 0.0004
200 °C	\\	1.17±0.03	0.0140±0.0009
-144 °C	0.040±0.004	1.072±0.011	0.0252±0.0005

Table 3.2: Parameters obtained by the exponential fit of the MoS_2 AES signal. For T_{amb} and 200 °C an estimation of y_0 was not possible.

moreover the two curves relative at the high temperatures do not show a big difference despite the 100 °C gap between the two cases. This was symptomatic of a defect in the high power supply controlling the energy selection of the Auger electrons.

Unfortunately, LEED images are not sharp enough to see eventually other structures apart from the hexagonal pattern associated to MoS_2, figure 3.19. It must be said that when cleaving MoS_2 a lot of flakes are left behind. Thus it is very difficult to have large areas of flat surface, which would be convenient for LEED measurements.

The results suggest further studies in order to clarify the origin of the islands observed in the STM and of the flat feature which was previously interpreted as a silicene layer. This hypothesis is hampered also by the AES spectra which show a layer-by-layer growth only at T=-144°C. It would be interesting to perform STM at low temperature to see if the silicon atoms arrange themselves in an ordered manner.
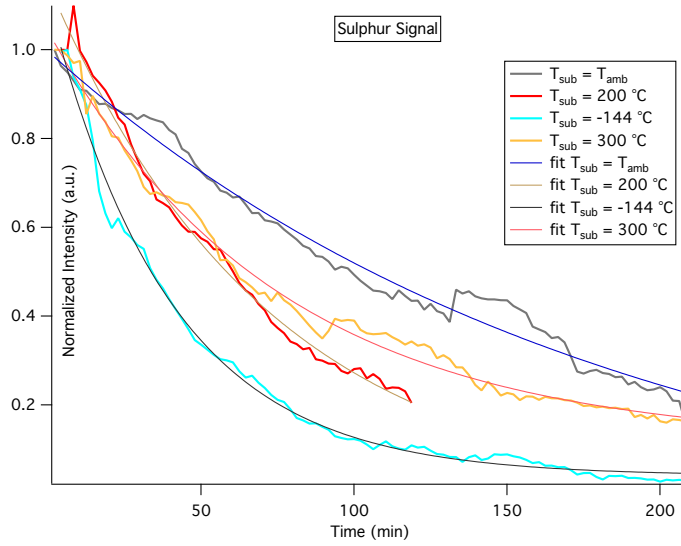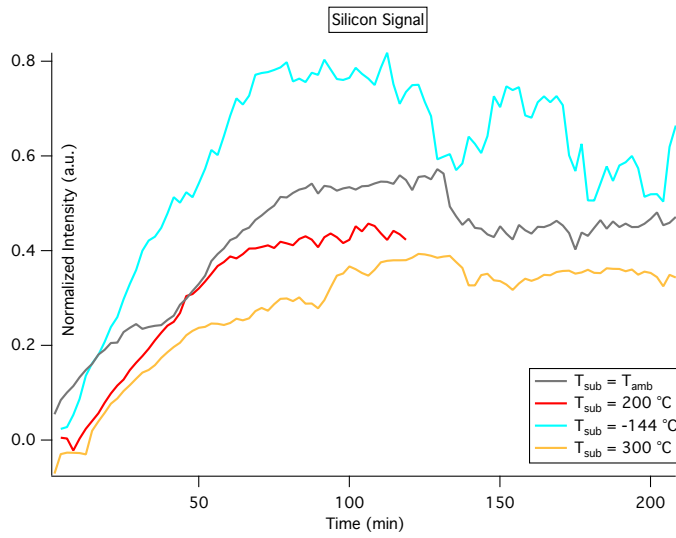
Figure 3.18: Evolution of the AES signal of S, relative to the MoS$_2$ substrate and of the Si deposited.
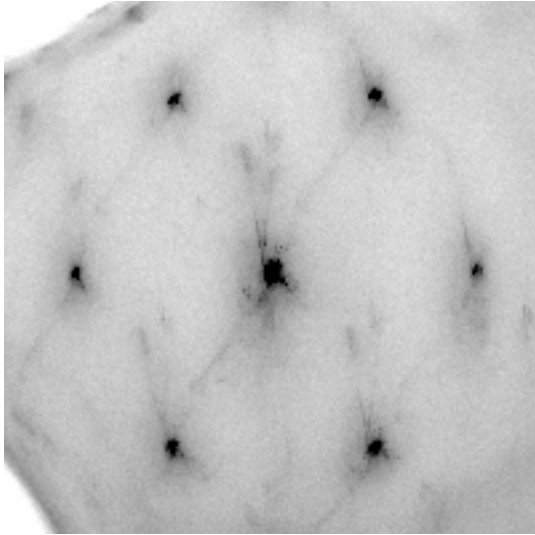
Figure 3.19: Example of LEED image taken after Si evaporation at 200 °C. The only evident pattern is the hexagonal one related to the bare MoS_2 structure.

Conclusions and further experiments

The experiments performed during my internship managed to shed some light on controversial observations made in the last years.

- *Bibliographic introduction: theoretical studies and first experimental observations*

  First of all a bibliography work has been necessary in order to gather all the basic information about silicene. DFT works shows that free standing silicene is arranged in a honeycomb low-buckled structure. It is predicted to show a linear dispersion curve at the K-point of the first Brillouin zone, where the electrons behave like massless Dirac fermions. According to different model $v_f \sim 10^{-6}$-10^{-5} m/s [5]. The first experimental works concern Ag(110), on which mono-dimensional nanoribbons have been observed. Anyway their silicene nature have been questioned by STM, GIXD and SDRS measurements, which show a reconstruction of the silver surface induced by silicon evaporation and different optical response from the one predicted. Ag(111) seemed to be a perfect candidate for silicene growth. In fact several works reports 2D silicon layers with different reconstructions of the surface observed on such a substrate. Further studies have demonstrated that Si evaporation affect strongly the silver substrate, making questionable the silicene nature of the structure observed. Finally for thick Si deposit, it has been observed an unexpected $\sqrt{3}$x$\sqrt{3}$ reconstruction of the surface after silicon evaporation. In a first moment it had been interpreted as a new reconstruction of silicene, but subsequent investigations has shown a migration of the silver atoms towards the surface suggesting that what it is observed could be the Si(111)$\sqrt{3}$x$\sqrt{3}$-Ag reconstruction. At the end of the first chapter I have discussed a paper

showing interesting results of silicon evaporation on MoS_2. The silicon features observed are interpreted as a highly buckled silicene layer. Anyway the results presented relies only on STM, STS and RHEED measurements. Thus, to reach more conclusive results more experiments are recommended.

I present now a summary of the results obtained evaporating silicon on four different substrate: Ag(111), HOPG, Si(111) 7x7-H, MoS_2.

- *Si/Ag(111)*

  In order to prove or disprove the involvement of silver atoms in the $\sqrt{3}x\sqrt{3}$ reconstruction AES and LEED measurements have been performed. It have been observed that even for thick Si deposition at $\gtrsim 200$ °C the AES signal of silver doesn't go to zero. It is clear than that Ag atoms are segregated in proximity of the surface, supporting the idea of their involvement in the $\sqrt{3}x\sqrt{3}$ reconstruction, observed with LEED. Eventually, SDRS at 206 °C and TR measurements showed that the optical response of the silicon deposited onto the Ag(111) is in good agreement with what is expected for bulk silicon, excluding the presence of silicene multi-layers. Now, to complete the picture, it would be very interesting to perform GIXD, in order to determine both qualitatively and quantitatively the role of silver in the $\sqrt{3}x\sqrt{3}$ reconstruction and extract a model from the results. This should have been done during the internship, but it has been delayed in September because of technical problems at the synchrotron facility. Moreover, studying SDRS and TR of thin silver film deposited on Si(111) could shed some light onto the role of surface silver atoms in the optical response of Ag(111) with thick Si deposition.

- *Si/HOPG*

  In the quest for silicene, new substrates must be tried out and studied, in order to find one which can accommodate this 2D silicon structure without interacting too strongly with it. Due to its hexagonal arrangement and its layered structure, HOPG has been chosen as a suitable candidate. STM measurements have shown a Volmer-Weber growth. From STM observation

it has been observed that also at low temperature, islands induced by silicon deposition grow on the surface. This is further confirmed by AES measurements in which the C signal after long Si deposition does not saturate to zero. The STM images do not show any atomically resolved structure, thus another STM session would allow a better characterization of the nature of the islands observed. AES and LEED measurements can also play a fundamental role for a better understanding of the phenomenon.

- *Si/Si(111)7x7-H*

  Si(111) has been probably the most disappointing substrate used, because the difficulties faced during the hydrogenation of the 7x7 reconstruction. The eventuality of trying hydrogenation by chemical attack has been taken into consideration, provided we can find someone available to show us the correct and safe way to do it using HF acid. In any case the hydrogenated surface is not perfectly stable in air and it is hard to say a priori if the transfer inside the chamber can be done fast enough to retain a good surface. The only Si evaporation performed hasn't shown any ordered silicon structure, but, as already said, the poor state of the surface played a drastic role in the experiments.

- *Si/MoS$_2$*

  Eventually, I performed STM, AES and LEED on MoS$_2$ during and after Si evaporation. STM images, after evaporation at RT, showed several interesting features: $\sim$0,1 nm and $\sim$2 nm high islands, a big feature of 5 nm high with unexpected straight edges and flat feature very similar to the ones reported in the literature [25]. The tip state has not allowed to discern uncontroversially the morphology of these structure. The most important observation regards the flat structure. In fact the step height of 3 Å is contradiction with the high-buckling model proposed in the literature by Chiappe et al. [25]. Moreover the tip seems to induce a dragging effect which suggests that the structure is highly unstable. The AES spectra during evaporation show a 2D growth at low temperature (T=-144 °C) and a 3D island growth at T=300 °C. At RT and T=200 °C the noise has not allowed to evaluate correctly

the saturation trend. Also the LEED images do not show any additional pattern to the hexagonal one identified for MoS_2 structure. Probably other measurements can be performed in more controlled conditions. In particular, it would be convenient to work on samples with large flat areas and to change the supply of the Auger apparatus which probably has caused the noise observed in the spectra.

Looking at future perspectives, more experiments on HOPG and MoS_2 would clarify some observations done during this internship: the nature and structure of the islands in both cases, the real origin of the flat feature observed on MoS_2. Concerning Si(111), the difficult process of hydrogenation and the lack of interesting results discourage further investigations, but the possibility of hydrogenation by chemical attack can be taken into consideration. Lately, I have spent some time looking for other possible substrate with a layered structure, honeycomb structure and lattice constant similar to silicene. Among the materials examined $TiTe_2$ and $ZrSe_2$ present a lattice constant of 3,77 nm very close to the one expected for free-standing silicene, 3,840 nm.

The quest for silicene is far from being close to an end. Both from an experimental and theoretical point of view, a lot of effort is nowadays spent to observe and better characterize this very promising and fascinating material.

Appendix A

Here is a schematics of the preparation chamber of the STM apparatus, which can help to have an idea of how the UHV conditions have been achieved and how the different substrates and the tips have been prepared.
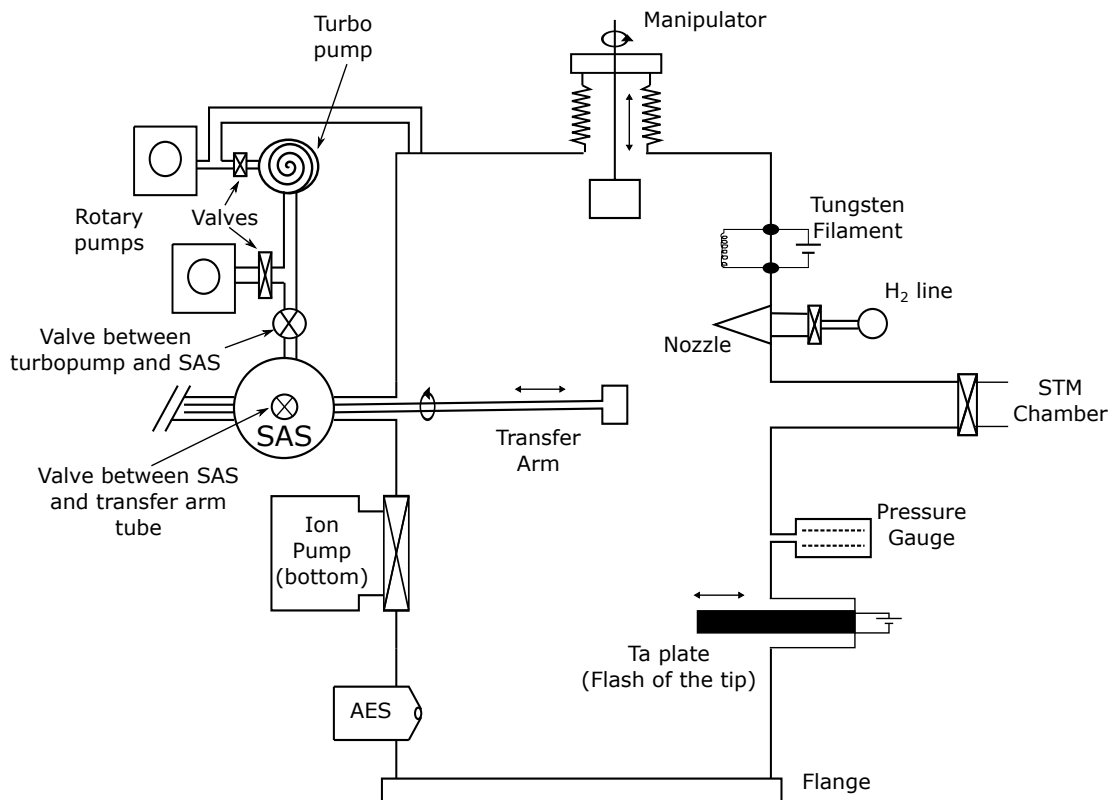
Appendix B

A very simple model is used for the estimation of the quantity of silver migrated ontop of the silicon atoms evaporated onto Ag(111). Basically, I consider a the Ag(111) substrate on which is presenta certain amount of silicon and, at the very top, a film of a certain thickness of silver, figure . The signal S coming from silver
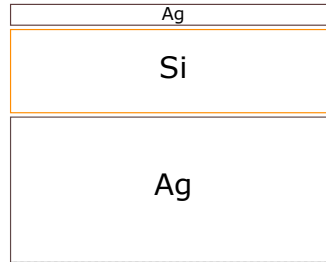

Figure 3.20: Sketch of the system studied.

is proportional to the summation of the contributions of all the Ag layers:

$$S \propto \sum_{n=0}^{N} exp(-n\frac{t}{\lambda}) \tag{3.2}$$

where t=0,334 nm is the thickness of one silver layer at 45° of incidence, N is the total number of layers and λ=0,54 nm [41] is the inelastic mean free path of ~350 eV electrons in silver. For N$\longrightarrow \infty$, the signal for bulk silver is obtained.:

$$S_{Ag-bulk} = \frac{1}{1 - exp(-\frac{t}{\lambda})} = 0,533 \tag{3.3}$$

This corresponds to 1 in the normalized intensities of AES spectra. Taking this into consideration a simple proportion can be used to estimate the fraction of Ag

layer deposited:

$$Si_{Ag-bulk} : 1 = Q_{Ag} : y_0 \tag{3.4}$$

from which we obtain, using the y_0 at the two different temperature, Q^{235}_{Ag}=(0,347±0,004) ML and Q^{205}_{Ag}=(0,278±0,004) ML.

Bibliography

[1] Yves Borensztein, Alberto Curcella, Sébastien Royer, and Geoffroy Prévot, *Silicene multilayers on Ag(111) display a cubic diamondlike structure and a $\sqrt{3} \times \sqrt{3}$ reconstruction induced by surfactant Ag atoms*, Phys. Rev. B, accepted 11/09/2015.

[2] K. S. Novoselov, A. K. Geim, S. V. Morozov, D. Jiang, Y. Zhang, S. V. Dubonos, I. V. Grigorieva, and A. A. Firsov, *Electric Field Effect in Atomically Thin Carbon Films*, Science 22 October 2004: 306 (5696), 666-669

[3] Hamid Oughaddou, Hanna Enriquez, Mohammed Rachid Tchalala, Handan Yildirim, Andrew J. Mayne, Azzedine Bendounan, Gérald Dujardin, Mustapha Ait Ali, Abdelkader Kara, *Silicene, a promising new 2D material*, Progress in Surface Science, Volume 90, Issue 1, February 2015, Pages 46-83.

[4] G.G. Guzman-Verri, L.C.L.Y. Voon, *Electronic structure of silicon-based nanostructures*, Phys. Rev. B 76 (2007) 075131.

[5] S. Cahangirov, M. Topsakal, E. Akturk, H. Sahin, S. Ciraci, *Two- and one-dimensional honeycomb structures of silicon and germanium*, Phys. Rev. Lett. 102 (2009) 236804.

[6] Choongyu Hwang, David A. Siegel, Sung-Kwan Mo, William Regan, Ariel Ismach, Yuegang Zhang, Alex Zettl, Alessandra Lanzara,*Fermi velocity engineering in graphene by substrate modification*, Scientific Reports 2, 590 (2012)

[7] A. Kara, H. Enriquez, A.P. Seitsonen, L.C.L.Y. Voon, S. Vizzini, B. Aufray, H. Oughaddou, *A review on silicene – new candidate for electronics*, Surf. Sci. Rep. 67 (2012) 1–18

[8] *Future Markets sees a USD 25-45 million graphene materials market in 2015*, graphene-info.com, 21 may 2015.

[9] H. Sahin, J. Sivek, S. Li, B. Partoens, F.M. Peeters, *Stone-wales defects in silicene: formation, stability, and reactivity of defect sites*, Phys. Rev. B 87 (2013) 085444

[10] Vogt, Patrick and De Padova, Paola and Quaresima, Claudio and Avila, Jose and Frantzeskakis, Emmanouil and Asensio, Maria Carmen and Resta, Andrea and Ealet, Bénédicte and Le Lay, Guy, *Silicene: Compelling Experimental Evidence for Graphenelike Two-Dimensional Silicon*, Phys. Rev. Lett. 108 (2012) 155501

[11] C. Léandri, G. Le Lay, B. Aufray, C. Girardeaux, J. Avila, M.E. Davila, M.C. Asensio, C. Ottaviani, A. Cricenti, *Self-aligned silicon quantum wires on Ag(110)*, Surf. Sci. 574 (2005) 9–15.

[12] M.R. Tchalala, H. Enriquez, A.J. Mayne, A. Kara, G. Dujardin, M. Ait Ali, H. Oughaddou, *Atomic structure of silicene NRs on Ag(110)*, J. Phys: Conf. Ser. 491 (2014) 012002

[13] B. Aufray, A. Kara, S. Vizzini, H. Oughaddou, C. Leéandri, B. Ealet, G. Le Lay, *Graphene-like silicon NRs on Ag 1 1 0: a possible formation of silicene*, Appl. Phys. Lett. 96 (2010) 183102

[14] R. Bernard, T. Leoni, A. Wilson, T. Lelaidier, H. Sahaf, E. Moyen, L. Assaud, L. Santinacci, F. Leroy, F. Cheynis, A. Ranguis, H. Jamgotchian, C. Becker, Y. Borensztein, M. Hanbucken, G. Prévot, L. Masson, *Growth of Si ultrathin films on silver surfaces: evidence of an Ag(110) reconstruction induced by Si*, Phys. Rev. B 88 (2013) 121411

[15] Borensztein, Yves and Prévot, Geoffroy and Masson, Laurence, *Large differences in the optical properties of a single layer of Si on Ag(110) compared to silicene*, Phys. Rev. B 89 (2014) 245410

[16] Olesinski, R.W., A Gokhale, A.B., A Abbaschian, G.J., *The Ag-Si (Silver-Silicon) system*, Bulletin of Alloy Phase Diagrams, Springer, 1989

[17] B. Lalmi, H. Oughaddou, H. Enriquez, A. Kara, S. Vizzini, B. Ealet, B. Aufray, *Epitaxial growth of a silicene sheet*, Appl. Phys. Lett. 97 (2010) 223109.

[18] Z. Majzik, M. Rachid Tchalala, M. Švec, P. Hapala, H. Enriquez, A. Kara, A. J. Mayne, G. Dujardin, P. Jelínek, H. Oughaddou, *Combined AFM and STM measurements of a silicene sheet grown on the Ag(111) surface*, Journal of Physics: Condensed Matter, 25 22 (2013) 225301

[19] P. Vogt, P. De Padova, C. Quaresima, J. Avila, E. Frantzeskakis, M.C. Asensio, A. Resta, B. Ealet, G. Le Lay, *Silicene: compelling experimental evidence for graphene like two-dimensional silicon*, Phys. Rev. Lett. 108 (2012) 155501

[20] H. Jamgotchian, Y. Colignon, N. Hamzaoui, B. Ealet, J.Y. Hoarau, B. Aufray, J.P. Biberian, *Growth of silicene layers on Ag(111): unexpected effect of the substrate temperature*, J. Phys.: Condens. Matter 24 (2012) 172001

[21] P. Vogt, P. Capiod, M. Berthe, A. Resta, P. De Padova, T. Bruhn, G. Le Lay, B. Grandidier, *Synthesis and electrical conductivity of multilayer silicone*, Appl. Phys. Lett. 104 (2014) 021602

[22] T. Shirai, T. Shirasawa, T. Hirahara, N. Fukui, T. Takahashi, and S. Hasegawa, *Structure determination of multilayer silicene grown on Ag(111) films by electron diffraction: Evidence for Ag segregation at the surface* Phys. Rev. B 89, 241403 (2014).

[23] Baojie Feng, Zijing Ding, Sheng Meng, Yugui Yao, Xiaoyue He, Peng Cheng, Lan Chen, and Kehui Wu, *Evidence of Silicene in Honeycomb Structures of Silicon on Ag(111)*, Nano Lett. 2012, 12, 3507-3511

[24] Prévot, G. and Bernard, R. and Cruguel, H. and Borensztein, Y., *Monitoring Si growth on Ag(111) with scanning tunneling microscopy reveals that silicene structure involves silver atoms*, Applied Physics Letters, 105, 213106 (2014)

[25] Chiappe, Daniele, et al. *Two Dimensional Si Nanosheets with Local Hexagonal Structure on a MoS2 Surface*, Advanced Materials 26.13 (2014): 2096-2101.

[26] A. V. Nezhdanov, D. O. Filatov, D. A. Antonov, S. Yu. Zubkov, A. I. Mashin, and A. V. Ershov, *The Morphology, Electron Structure, and Optical Properties of Self-Assembled Silicon Nanostructures on the Surface of Highly Oriented Pyrolytic Graphite*, Surfaces, Interfaces and Thin Films, ISSN 10637826, 2011

[27] H. Lüth, *Surfaces and Interfaces of Solids*, Springer-Verlag, Berlin, 1993

[28] *Fundamentals of Vacuum Technology*, Oerlikon Leybold Vacuum, Cologne, 2007

[29] *Variable Temperature UHV SPM*, Omicron NanoTechnology GmbH, Oxford Instruments Group

[30] Anne-Sophie Lucier, *Preparation and Characterization of Tungsten Tips Suitable for Molecular Electronics Studies*, Center for the Physics of Materials Department of Physics, McGill University, Montréal, Québec, Canada, February 2004

[31] Peter Y. Yu, Manuel Cardona, *Fundamentals of Semiconductors: Physics and Materials Properties*, Third Edition, Springer, Berlin, 2005

[32] *Instruction Manual SPA-LEED*, Omicron Instruments for Surface Science, Oxford Instruments Group

[33] McIntyre, J. D. E., and D. E. Aspnes, *Differential reflection spectroscopy of very thin surface films*, Surface Science 24.2 (1971): 417-434.

[34] G. E. Jellison and F. A. Modine, Phys. Rev. B 27, 7466 1983

[35] E. Matatagui, A. G. Thompson, and M. Cardona, Phys. Rev. 176, 950 (1968)

[36] G. E. McGuire, *AUGER ELECTRON SPECTROSCOPY REFERENCE MANUAL*, Texas Instruments Inc., Springer, Dallas, Texas, 1979

[37] Kobayashi, Yousuke, et al., *Observation of zigzag and armchair edges of graphite using scanning tunneling microscopy and spectroscopy.*, Physical Review B 71.19 (2005): 193406

[38] H. Neddermeyer, *Scanning tunnelling microscopy of semiconductor surfaces.*, Fachbereich Physik, Martin-Luther-Universitat Halle-Wittenberg, Germany, 1996

[39] F. Owman, P. Martensson, *STM study of structural defects on in situ prepared Si(111) 1 × 1-H surfaces*, Surface Science Letters 303, 1994

[40] Stupian, Gary W. and Leung, Martin S., *Imaging of MoS2 by scanning tunneling microscopy*, Applied Physics Letters, 51, 1560-1562 (1987), DOI:http://dx.doi.org/10.1063/1.98635

[41] NIST Electron Effective-Attenuation-Length Database, http://www.nist.gov/srd/nist82.cfm